Changes and variability of precipitation and temperature in the Ganges-Brahmaputra-Meghna River Basin based on global high-resolution reanalyses

Khandu[a], Joseph L. Awange[a,b], Michael Kuhn[a], Richard Anyah[c], Eshan Forootan[d,e]

[a] *Western Australian Centre for Geodesy and the Institute for Geoscience Research, Curtin University, Western Australia, Australia*
[b] *Department of Cartographic Engineering, Universidade Federal de Pernambuco, Recife, Pernambuco, Brazil*
[c] *Associate Professor, Department of Natural Resources and the Environment, University of Connecticut, Storrs, Connecticut, USA*
[d] *Institute of Geodesy and Geoinformation, University of Bonn, Bonn, Germany*
[e] *School of Earth and Ocean Sciences, Cardiff University, Cardiff, UK*

Abstract

Many previous studies have suggested that climate change impacts significantly on the hydro-climatic processes within the Ganges-Brahmaputra-Meghna (GBM) River Basin (RB). This study examines the observed climate characteristics and potential strengths and limitations of recent global high-resolution reanalyses and satellite remote-sensing (SRS) products over the GBM RB for the most recent period (1980-2013) by (i) estimating trends and interannual variations of precipitation and temperature and (ii) isolating precipitation variations likely associated with El Niño Southern Oscillation (ENSO) and Indian Ocean Dipole (IOD). The surface temperature trends show widespread warming across the basin with a maximum increase of 0.6°C/decade over western Nepal and southern Tibet from 1980–2013. Rainfall changes over 1980–2013 indicated pronounced decline over high rainfall regions of northeast India, Bhutan, Nepal, and Bangladesh, especially from 1998–2013. Basin-averaged trends show rainfall declines of up to 39 mm/decade in June-August in the Brahmaputra-Meghna RB from 1998–2013. Temperature variability based on Principal Component Analysis (PCA) indicates that the first mode is associated with sea surface temperature (SST) warming in the Arabic Sea and the western tropical Pacific

Email address: Khandu@postgrad.curtin.edu.au (Khandu)

Ocean, while the second mode appears to be significantly correlated to SST anomalies in the western (eastern) tropical Indian (Pacific) Ocean. The results also indicate that ENSO and IOD events significantly influence rainfall variability, contributing to about 10–20% (ENSO) and 8–10% (IOD) to the annual rainfall, mainly over the Bhutan, Nepal, Bangladesh, and northeastern India. The quality of reanalysis products is highly variable over the GBM RB. MERRA (Modern-Era Retrospective Analysis for Research and Applications) agrees well with observed temperature data from the Climate Research Unit (CRU TS3.22), while ERA-Interim appears closer to observed precipitation datasets. Climate Forecast System Reanalysis (CFSR) shows the least seasonal and interannual skills among the three products.

Keywords: Ganges-Brahmaputra-Meghna River Basin, climate, reanalysis, satellite remote-sensing, precipitation, temperature

---

1. Introduction

Estimating long-term trends in surface air-temperature (hereinafter called "temperature") and precipitation are crucial for identifying climate change. Precipitation and temperature are two critical components of the water and energy cycles, and precipitation in particular, due to its high spatio-temporal variability, is one of the most difficult fluxes to simulate in dynamical models (*Flato et al.*, 2013). So, as critical as it is in the water and energy cycles, precipitation is a critical metric in the quality of many existing and emerging retrospective analyses (reanalyses). Evaluating climate models require consistent long-term observational records. Hydrological or land surface models, in particular, require high quality of climate forcing data (e.g., precipitation) to simulate other components of the water balance (e.g., soil moisture, (sub-) surface runoff) terms. Satellite remote-sensing (SRS)-based estimates and reanalyses offer an alternative approach to *in-situ* observations where gauge-based networks are sparse and their analyses are often delayed or not shared across a common hydrological basin (*Duncan and Biggs*, 2012; *Peña-Arancibia et al.*, 2013).

Reanalysis outputs are generated by forecast models with fluxes constrained by available gauge- and SRS-based observations, and thus are sensitive to both the observing systems and model physics. The release of several global reanalyses over the past two decades (e.g., *Kalnay et al.*, 1996; *Onogi et al.*, 2005; *Uppala et al.*, 2005; *Onogi et al.*, 2007; *Saha et al.*, 2010; *Dee et al.*, 2011; *Rienecker et al.*, 2011), provided several decades of various hydro-climatic data that are highly valuable for understanding the global/regional climate change process. The most widely used reanalysis products include those developed at the National Centers for Environmental Prediction (NCEP)/National Center for Atmospheric Research (NCAR) (see, *Kalnay et al.*, 1996; *Kanamitsu et al.*, 2002), and at the European Center for Medium-Range Weather Forecasts (ECMWF) (see, *Uppala et al.*, 2005; *Dee et al.*, 2011). Japan Meteorological Agency (JMA) and the Central Research Institute of Electric Power Industry (CRIEPI) have released two versions of reanalyses (JRA-25 and JRA-55) with the goal of providing consistent and high-quality reanalysis specifically over Asia (*Onogi et al.*, 2005, 2007; *Kobayashi et al.*, 2015). More recently, the National Aeronautic and Space Administration (NASA) has produced a global high-resolution reanalysis called the Modern-Era Retrospective Analysis for Research and Applications (MERRA, *Rienecker et al.*, 2011) covering the satellite-era, while NCEP produced another high-resolution reanalysis called the Climate Forecast System Reanalysis (CFSR, *Saha et al.*, 2010).

While reanalysis products are considered to be near-perfect representations of the atmospheric state, they suffer from many deficiencies at various time- and spatial-scales. Considering that many global high-resolution reanalyses have become available during the past few years (e.g., *Saha et al.*, 2010; *Dee et al.*, 2011; *Rienecker et al.*, 2011), it is vital to evaluate their skills in terms of how they represent key climate features over different parts of the world. The spatio-temporal heterogeneity of orography and climate (particularly, precipitation) of the Ganges-Brahmaputra-Meghna (GBM) River Basin (RB) in South Asia presents one of the most challenging tests to any observing and modelling systems. The Indian summer monsoon, which dominates the annual rainfall

contribution (by 60–90%) is a result of complex interplay between the atmosphere, land, and the Indian ocean processes that takes place at various spatial- and temporal-scales. The pressure gradients that is formed between the south and north Indian ocean leads to a cross-equatorial flow in the lower troposphere, which carries enormous moisture towards the Indian sub-continent. These monsoon rainfall pattern is further modulated by steep mountains of the Himalayas (*Barros et al.*, 2004) along various stages of its flow in the GBM RB, resulting in numerous high rainfall spots and dry regions.

Only few studies have assessed the quality of rainfall and temperature variability of reanalysis products over the GBM River Basin, with all of them focussing over India and during the monsoon season (*Misra et al.*, 2012; *Kishore et al.*, 2016). *Kishore et al.* (2016) indicated that ECMWF reanalysis (ERA-Interim, *Dee et al.*, 2011) was more closer to observed values than MERRA, CFSR, and JRA-25 during the monsoon season between 1989 and 2007. In another comparison study, *Misra et al.* (2012) indicated that there are significant differences in the climatology of evaporation in the three reanalyses: CFSR, MERRA, and NCEP II, which will have huge implications on precipitation and temperature across South Asia. Particularly, the study found significantly less continental evaporation in CFSR compared to MERRA and NCEP II, which may be attributed to how each reanalyses treat the atmospheric-land interactions. These results suggest that reanalysis products are still evolving and requires continuous validation over the Indian monsoon region.

This study examines the long-term trends and interannual variability of rainfall and temperature over the GBM RB, using various existing gridded gauge-based datasets, and global high-resolution reanalyses over the period 1980–2013. The primary objective here is to assess the quality of three global high-resolution reanalyses: (i) ERA-Interim [$0.79^\circ \times 0.79^\circ$], (ii) MERRA [$0.50^\circ \times 0.67^\circ$], (iii) CFSR [$0.50^\circ \times 0.50^\circ$], in estimating the long-term trends and the interannual variability of rainfall and temperature, which are important metrics for identifying climate change. The study is complemented by two SRS-based precipitation estimates: (i) Tropical Rainfall Measuring Mission (TRMM) Multisatellite

Precipitation Analysis (TMPA, 1998-2014) (*Huffman et al.*, 2007) and (ii) Climate Hazards Group InfraRed Precipitation (CHIRP, 1982-2014) (*Funk et al.*, 2012), both of which have a relatively long period of precipitation records. Many studies have already examined the seasonal skills of various existing SRS-based precipitation estimates across different parts of the GBM RB (e.g., *Andermann et al.*, 2011; *Duncan and Biggs*, 2012; *Prakash et al.*, 2014; *Khandu et al.*, 2016a), but have not addressed their long-term skills. Gauge-based datasets used here include: Asian Precipitation Highly Resolved Observational Data Integration Towards Evaluation of Water Resources (APHRODITE V1101, *Yatagai et al.*, 2012), Climate Research Unit (CRU TS3.22, *Harris et al.*, 2013), and Global Precipitation Climatology Centre (GPCC version 6, *Schneider et al.*, 2014).

Section 2 describes the climatological characteristics of the GBM RB. In Section 3, a brief review of the available rainfall and temperature datasets is presented as well as the statistical methods used to analayse and compare the various datasets. It also discusses the accuracy of several near-global high-resolution SRS-based precipitation products in the region and their contribution to the understanding of basin rainfall hydrology. The results are presented and discussed in Section 4 and Section 5 concludes the study.

2. The Ganges-Brahmaputra-Meghna (GBM) River Basin (RB)

The GBM RB in South Asia is a combination of three large river basins with a drainage area of about 1.7 million km^2 (*FAO*, 2011). Although the three river basins have distinct physiological and climatological characteristics even, it is considered to be one river basin that is shared by India (64%), China (18%), Nepal (9%), Bangladesh (7%) and Bhutan (3%) (Fig. 1). The three river systems join upstream of the GBM delta in Bangladesh to form the third largest freshwater outlet (with a annual discharge of ∼1,350 km^3) to the world's oceans, being exceeded only by the Amazon and the Congo river systems (*Chowdhury and Ward*, 2004; *Steckler et al.*, 2010). The headwaters of Ganges (Brahmaputra) rivers originate from the Himalayan mountains of Gan-

gotori glaciers (northern slope of the Himalayas in Tibet) while the Meghna river, originates in the mountains of north-eastern India. The Ganges is joined by several smaller rivers (or tributaries) from across India and Nepal forming one of the largest alluvial plains in northern India. A portion of Ganges river (∼50%) is diverted into the Hooghly river at Farakka Barrage before reaching Bangladesh as a part of a treaty (called Farakka Treaty) signed between India and Bangladesh in 1996 to share the precious Ganges river (see, http://www.thewaterpage.com/farakka_water_treaty.htm).

[FIGURE 1 AROUND HERE.]

The Brahmaputra river, also known as Yarlung Tsangpo (in Tibet), flows eastwards before turning southwards into Arunachal Pradesh (India). It then turns westwards, which is joined by many tributaries from northeast India and Bhutan, before entering Bangladesh (also called Jamuna). The Meghna river originates from the hilly mountains of Manipur (India), flowing southwest to join the Ganges and Brahmaputra rivers that together flow into the Bay of Bengal and a small part of West Bengal (India) forming the greatest deltaic plain in the world at the confluence.

The GBM RB features distinct climatic characteristics due to the Indian monsoon variability and unique topographic regime that includes the Himalayan mountains and great plains of Ganges, Terai, parts of northeast India, and Bangladesh. These irregular topographic variations significantly impact on the spatial precipitation distribution through alteration of monsoonal flow, resulting in pronounced orographic rainfall along the Southern Foothills of Nepal, Bhutan and northeast India and considerably lower rainfall on the lee sides of the mountains and the western Ganges RB. The Ganges RB is characterized by significant snowfall and precipitation in the northwest of its upper region and very high precipitation in the areas downstream regions (such as the delta regions of Bangladesh). The downstreams areas of Brahmaputra RB are directly located on the monsoon flow and hence, some of the areas receive significantly higher rainfall than the Ganges, while the world's highest precipitation is re-

ceived at Cherapunji (Meghalaya, India) located in the Meghna RB.

The winter precipitation over the western Himalayas is mainly driven by the mid-latitude sub-tropical jets known as the Western Disturbances, which is critical to the formation of snow/glaciers (*Dimri et al.*, 2015). While the winter precipitation is well below 50 mm (as shown in Fig. 2a), the Indian monsoon accounts for 60-90% of the annual rainfall total in the GBM RB recording over 1200 mm/month from June to September over Meghalaya (India) and southwest of Bhutan (Fig. 2b). The vector plots of winds (at 850 hPa pressure level) in Fig. 2 indicates the climate dynamics of the region e.g., winter (monsoon) precipitation is mainly forced by the westerlies of the Arabic Sea (southerlies of the Indian monsoon). The spatial temperature distribution is a function of altitude that decreases from as high as 40s (°C) during summer in the plains (e.g., Bangladesh) to as low as -30s (°C) in the Himalayas during winter. In this study, the Brahmaputra and Meghna RBs are treated as one river basin wherever a basin-average is calculated. The reason for merging them is that even though they have distinct climatological behaviours, they are affected by the monsoon at the same time.

[FIGURE 2 AROUND HERE.]

3. Data and methods

3.1. Available observational data

Accurate and reliable estimation of precipitation requires dense gauge or radar networks that are not easily achievable in rugged Himalayan mountain regions (e.g., Bhutan and Nepal). Thus, gridded precipitation products based on *in-situ* observations may not accurately estimate rainfall where these gauge networks are sparse (e.g., *Duncan and Biggs*, 2012; *Khandu et al.*, 2016a). Figure 3 shows the spatial distribution of rain gauges over GBM RB that were used to derive (a) APHRODITE V1101 (hereinafter as APHRODITE), (b) CRU version TS3.22 (hereinafter as CRU_TS3.22), and (c) GPCC version 6 (hereinafter as GPCCv6). It is evident from Fig. 3 that gauge density is sparse across the GBM

RB, especially in the Tibetan region, western Ganges, Bhutan, Bangladesh, and northeast India. CRU_TS3.22 has the least amount of stations (Fig. 3b).

[FIGURE 3 AROUND HERE.]

The accuracy of APHRODITE product was quantitatively evaluated across various parts of the GBM RB including Bhutan, Nepal, and India by various studies (e..g., *Rajeevan and Bhate*, 2008; *Andermann et al.*, 2011; *Xue et al.*, 2013; *Prakash et al.*, 2015; *Khandu et al.*, 2016a). *Andermann et al.* (2011) reported that APHRODITE shows the smallest error and high r-square values at both daily and monthly scales when compared to daily precipitation rates over Nepal. Comparison over India by *Rajeevan and Bhate* (2008) and *Prakash et al.* (2015) indicated that APHRODITE is well correlated (>0.6) with high-quality Indian Meteorological Department (IMD) daily precipitation ($1.0^\circ \times 1.0^\circ$ grid) data. Over Bhutan, *Khandu et al.* (2016a) found that APHRODITE was comparable to independently gridded precipitation estimates. All of these studies demonstrate that APHRODITE is a reliable product at least for the validation period. *Prakash et al.* (2015) evaluated several land-based precipitation data including APHRODITE, CRU_TS3.22, and GPCCv6 over India using high-density IMD rainfall data and indicated that APHRODITE and GPCCv6 were highly correlated with IMD data. The study also reported that GPCCv6 estimates were found to be quantitatively closer to IMD data during the monsoon, while APHRODITE precipitation estimates are found to be lower than GPCCv6 and IMD datasets (see also, *Yatagai et al.*, 2012).

Many global/near-global high-resolution SRS-based precipitation products have been released over the past decade with daily or finer temporal resolutions. Table 1 shows the details of various SRS-based precipitation products that have been applied across the GBM RB. The quality of these products have been investigated in a number of studies (e.g., *Yin et al.*, 2008; *Andermann et al.*, 2011; *Duncan and Biggs*, 2012; *Shrestha et al.*, 2012; *Xue et al.*, 2013; *Prakash et al.*, 2014; *Khandu et al.*, 2016a). These studies suggest that SRS-based estimates generally underestimate monsoon rainfall. Their limited

skills in detecting rainfall over rain-shadow regions and generally overestimating daily rainfall amounts over high-altitude regions is also reported in e.g., *Andermann et al.* (2011); *Duncan and Biggs* (2012); *Prakash et al.* (2014). Based on these findings, APHRODITE (1979–2007), GPCC (1979–2010) and TMPAv7 (1998–2013) precipitation estimates (both daily and monthly) are used to examine the long-term trends and variability of precipitation over the GBM RB and for evaluating various reanalysis products over the region. As a compromise between spatial resolution and estimation of long-term trends among different precipitation products, TMPAv7 product were linearly interpolated (using inverse distance weighting function) to a $0.5^\circ \times 0.5^\circ$ grid resolution.

[TABLE 1 AROUND HERE.]

Currently, there exists several gridded temperature datasets derived from surface observations across the globe. A list of high-resolution gridded temperature datasets derived from *in-situ* observations are shown in Table 2. The daily mean (T_{ave}) gridded temperature data made available by APHRODITE is the only high-resolution ($0.25^\circ \times 0.25^\circ$) gauge-based product over Asia and covers the period from 1961–2007. A monthly time-series of gridded temperature data compiled from a recent version of the Global Historical Climatology Network (GHCN2) and several other sources has been released by the University of Delaware (UDEL, *Legates and Willmott*, 1990; *Willmott and Robeson*, 1995). The dataset (currently version 3.01, UDELv3.01) has been recently used by *Chowdary et al.* (2014) to study the impacts of large-scale atmospheric-ocean interactions on surface temperature over India. CRU regularly updates its global-land surface temperature data (see, *Harris et al.*, 2013) and is the mostly widely used temperature dataset globally.

[TABLE 2 AROUND HERE.]

3.2. Reanalysis products

Reanalyses have made significant contributions to the global/regional hydrological and climatic studies. With the release of many new high-resolution

reanalyses in the past decade (e.g., *Kalnay et al.*, 1996; *Onogi et al.*, 2007; *Saha et al.*, 2010; *Dee et al.*, 2011), their application into regional- and basin-scale studies have become increasingly valuable. Yet certain elements of the analyzed fields (e.g, precipitation) remain highly uncertain at global and regional scale both in terms of trends and interannual variabilities. The reliability of reanalysis fields can considerably vary in space and time due to lack of adequate observational data, instrumental changes, changing mix of observations, biases in observations, etc., which can introduce spurious variability and trends into reanalysis fields. Since reanalysis products are increasing used as regional climate forcing data and hydrological model inputs, it is vital to estimate their accuracies. A reanalysis system consists of (i) a "data assimilation system" that combines available observations from various data sources and (ii) a "forecast model" consisting of a atmospheric model at its core, which is often coupled to a land surface model and/or ocean model (e.g., *Kalnay et al.*, 1996; *Dee et al.*, 2011; *Onogi et al.*, 2007).

Many reanalysis products have been assessed using gauge-bsed observations over various parts of the GBM RB (e.g., *Peña-Arancibia et al.*, 2013; *Shah and Mishra*, 2014; *Forsythe et al.*, 2014; *Kishore et al.*, 2016). *Shah and Mishra* (2014) evaluated MERRA, ERA-Interim, and CFSR with observed data from IMD, APHRODITE and TMPAv7 and found a precipitation (temperature) bias of 10% (-0.39°C), 34% (-0.21°C), and 11% (-0.44°C), respectively, during the monsoon over the Indian subcontinent. These products also failed to reproduce the observed trends in the monsoon season precipitation and temperature over India. *Kishore et al.* (2016) reported that precipitation fields of ERA-Interim, MERRA, CFSR, and JRA-25 generally showed very good correlation with IMD data and captured the annual cycle reasonably well. However, these studies are carried out at continental scales and there is a urgent need to address their potential applications in hydro-climatic studies over the GBM RB. Three global atmospheric reanalyses namely, (a) ERA-Interim/Land (*Balsamo et al.*, 2015), hereinafter referred to as ERA-Interim only, (b) MERRA Land (*Rienecker et al.*, 2011), hereinafter referred to as MERRA only, and (c) CFSR (*Saha et al.*,

2010) were considered here mainly because of their improvement in simulating the land-surface state (see, Table 3 for details). These land-based reanalyses has been particularly designed to accurately simulate the land-surface state (moisture content/temperature) of soil, vegetation, and snow/ice to understand the impacts of climate change in recent years (*Rienecker et al.*, 2011; *Balsamo et al.*, 2015)

[TABLE 3 AROUND HERE.]

3.3. Sea surface temperature data

In order to determine the mechanisms for seasonal and interannual variabilities of rainfall and temperature, their time-series were correlated with the observed sea surface temperatures (SSTs) provided by the Met Office Hadley Centre, UK. The Hadley Centre Global Sea Ice and Sea Surface Temperature (HadISST, *Rayner et al.*, 2003) is a combination of monthly globally fields of SST and sea ice concentration covering the period 1871-present. The global-complete monthly HadISST data, which is provided at a $1^\circ \times 1^\circ$ grid, is developed using a complex process involving a reduced space optimal interpolation technique that is applied to SST data from the Marine Data Bank (mainly obtained through ship tracks) and International Comprehensive Ocean-Atmospheric Data Set (ICOADS) through to 1981. From here, these datasets are complemented by a blend of *in-situ* and adjusted SRS-derived SSTs. Where the SSTs are covered with ice, a different analysis is performed by combining sea ice data from historical charts from shipping, expeditions and other activities, passive microwave SRS retrievals, and NCEP operational ice analyses. Here, we use HadISST data from 1980–2013 covering 50°N-50°S.

In addition, two ocean-atmospheric indices were used covering the same period, namely: (a) Niño3.4 index (*Trenberth*, 1990) and (b) Dipole Mode Index (DMI, *Saji et al.*, 1999) to examine the impacts of natural climate variabilities such as El Niño Southern Oscillation (ENSO) and Indian Ocean Dipole (IOD), respectively. It should be noted that ENSO and IOD variability may also be

influenced by long-term changes due to e.g., climate change. ENSO is commonly measured by sea surface temperature (SST) anomalies in the equatorial Pacific ocean, typically over (5°N–5°S, 120°–170°W), which is also known as Niño3.4 region (see, *Trenberth*, 1990). ENSO events are said to occur if SST anomalies exceed 4°C for 6 months or more. Warm and cold ENSO phases are referred to as El Niño and La Niña events, respectively, which are represented by anomalous warming of the central and eastern tropical Pacific (warm phase), and vice versa. ENSO events are marked by significant variations in surface and upper-air conditions such as prolonged droughts and heavy rainfall events at the surface and anomalous warming or cooling of the upper-tropospheric lower-stratospheric (UTLS) region. Niño3.4 index was obtained from the National Oceanic and Atmospheric Administration (NOAA, see, `http://www.esrl.noaa.gov/psd/data/climateindices/list/`).

IOD is measured by the difference of SST anomalies between the western (50°E–70°E and 10°S–10°N) and eastern (90°E–110°E and 10°S–0°S) equatorial Indian ocean, which is also referred to as DMI. Positive IOD events are identified by a cooler than normal water in the tropical eastern Indian Ocean and warmer than normal water in the tropical western Indian Ocean. These positive IOD events are associated with a shift of active convection from eastern Indian Ocean to the west leading to potentially higher than normal rainfall over parts of the Indian subcontinent. DMI was obtained from the Japan Agency for Marine-Earth Science and Technology (see, `http://www.jamstec.go.jp/frsgc/research/d1/iod/`).

3.4. Statistical analyses

Monthly rainfall and temperature anomalies are calculated relative to the data period from e.g., 1980–2010 and long-term trends are estimated and tested using both *parametric* (e.g., *Helsel and Hirsch*, 2002, pp 221–264) and *non-parametric* (e.g. *Mann*, 1945; *Kendall*, 1962; *Sen*, 1968; *Hirsch and Slack*, 1984) methods. Parametric tests are considered to be more powerful but require data to be independent and normally distributed, which is rarely the case for climate

datasets. Non-parametric methods on the other hand, do not require the assumption of normality and therefore, are considered to be more robust. Thus, both parametric and non-parametric tests are applied here to robustly determine the trend estimates of precipitation and temperature. The two statistical methods are described in Appendix A1 and Appendix A2.

Further, both weather and climate are a result of complex non-linear interaction between various components of the Earth system and contain significant temporal and spatial correlations, which makes the physical interpretation difficult. Principal Component Analysis (PCA, *Preisendorfer*, 1988) is one of the widely used data exploratory tools used in atmospheric/oceanic science that allows for a space-time display of spatio-temporal data such as precipitation and temperature, in a very few modes. PCA is multipurpose and have been used in various geophysical and climatic applications for dimensionality reduction (or removing irrelevant small-scale signals/noise), pattern extraction, and comparison of different datasets (see, *Hannachi et al.*, 2007; *Forootan*, 2014, for a detailed review of its mathematical derivation and applications). PCA is applied here to isolate the likely influences of ENSO and IOD on the surface temperature changes in the GBM RB. A mathematical representation of the PCA method is briefly described in Appendix A3.

4. Results

4.1. Trend and amplitudes of rainfall and temperature

The mean annual amplitudes of monthly rainfall from gauge-based GPCCv6, SRS-based TMPAv7 and CHIRP, and three reanalysis products (i.e., ERA-Interim, MERRA, and CFSR) are shown in Fig. 4. Precipitation over the GBM RB shows significant spatial variability across all months as a result of the Indian monsoon and the orographic effects of the Himalayan mountains. The largest precipitation amplitudes are seen over the Brahmaputra-Meghna RB, while the Ganges RB show relatively low rainfall amplitudes except over few regions such as central Nepal (Fig. 4a–c). These annual amplitude maps closely relate the

average monsoon rainfall from June-September (JJAS) as indicated in Fig. 5. Note that the spatial patterns of JJAS rainfall is more localised, especially in the GPCCv7 data (Fig. 5a) indicating that SRS-based products depict a larger footprint (Fig. 5b–c). There are three regions: (a) Meghalaya, (b) southwest Bhutan, and (c) northern Arunuchal Pradesh that receive the highest monthly rainfall amount (∼1200 mm during the JJAS) and hence shows the largest amplitude in all the observed datasets (Fig. 4a–c). Both TMPAv7 and CHIRP (1998–2013) show similar magnitudes of annual maps as GPCCv6 (Fig. 4b–c) but substantially underestimate monsoon rainfall in the high rainfall regions (Fig. 5b–c), albeit for different periods.

[FIGURE 4 AROUND HERE.]

[FIGURE 5 AROUND HERE.]

However, reanalysis products (specifically ERA-Interim and MERRA) significantly underestimate the annual amplitude (Fig. 4d–e) and the JJAS rainfall amount (Fig. 5d–e). MERRA, in particular failed to generate rainfall structures over Nepal and along the coastal areas of the Bay of Bengal (Fig. 4e and 5e), while both ERA-Interim and MERRA can barely represent the monsoon rainfall (Fig. 5d–e). CFSR, on the other hand, highly overestimates the annual amplitude and also misplaces the high rainfall region of southwest of Bhutan towards the east (Fig. 4f and 5f). While a strong agreement between TMPAv7 and GPCCv6 is expected, the differences between GPCCv6 and reanalysis products (especially, ERA-Interim and MERRA) is striking, given that both products are adjusted with observed rainfall datasets. For example, MERRA underestimates annual amplitude by 21–37% over the GBM RB (Table 4). CHIRP and APHRODITE estimates are also considerably lower than the other observed products over the basin (Table 4), which has been noted by *Prakash et al.* (2015).

[TABLE 4 AROUND HERE.]

Figure 6 shows the spatial variability of surface temperature over the GBM RB (over the period 1980–2010) based on observed data (CRU_TS3.22 and UDEL) and three reanalysis products (ERA-Interim, MERRA, and CFSR). The annual amplitude of temperature increases with altitude with both CRU_TS3.22 and UDEL gauge datasets (Fig. 6a–b) showing considerably high (>8°C) variations in the Tibetan region (located entirely in the Brahmaputra RB) and parts of the western Ganges RB (Indian region). The temperature varies between 5°C and 8°C in western Nepal, northern Bhutan, and Arunuchal Pradesh (in India) while the lowest annual variations (∼5°C) are seen in Bangladesh and eastern India. The annual amplitude of temperature shown by the reanalysis products shows very similar spatial structures but their magnitudes varies considerably across the basin. While ERA-Interim tend to underestimate annual amplitudes (Fig. 6c), MERRA and CFSR products (Fig. 6d–e) overestimate annual amplitudes (by around 3–4°C) with respect to CRU_TS3.22 dataset, especially in the Ganges RB and in the Tibetan region. The basin averaged annual amplitudes (of temperature) are provided in Table 4, which indicates that MERRA depicts the largest annual variation followed by CFSR in the GBM RB. The maximum surface temperature over Ganges and Brahmaputra-Meghna basins occur during May and July, respectively, while their minimum temperatures occur in January.

[FIGURE 6 AROUND HERE.]

Changes in temperature and precipitation are estimated both in observations and reanalysis products for the period 1980-2010 using both parametric and non-parametric methods described in Section 3.4. However, precipitation trends are also calculated for the various time periods between 1980 and 2013 to shows the precipitation changes based on APHRODITE (1980-2007) and SRS-based (TMPAv7 and CHIRP) precipitation products. Rainfall trends between 1980 and 2007 are found to be negative (up to 10-15 mm/decade) mainly over the Ganges RB, consistently shown by all the observed products (i.e., APHRODITE, CRU_TS3.22, GPCCv6, results not shown). Figure 7 shows the

precipitation changes over the GBM RB based on GPCCv6 (1980–2010), TMPAv7 and CHIRP (1998–2013), and the three reanalyses (1980–2010). While the changes in GPCCv6 are similar to those between 1980 and 2010 (Fig. 7a), significant increasing (decreasing) trends are seen from 1998-2013 over the western Ganges (Brahmaputra-Meghna) RBs showing large decreases (of about 20-30 mm/decade) over Bangladesh, northeast India, western Nepal, and southwestern Bhutan (Fig. 7b–c). Between 1998 and 2013, both TMPAv7 and CHIRP indicate strong decline of rainfall over the years in the Brahmaputra-Meghna RB (39 mm/dec in TMPAv6 during June-August). However, the increasing trend (12 mm/decade by TMPAv7) found over the Ganges RB is not replicated in CHIRP (Table 5) as it shows few areas with increasing trends in the western Ganges RB (Fig. 7c).

[FIGURE 7 AROUND HERE.]

Among the reanalyses, ERA-Interim tends to capture the observed trends but their magnitudes are significantly larger over western Nepal and eastern India (Fig. 7d) compared to GPCCv6 (Fig. 7a), while MERRA and CFSR show completely opposite signs of change over the Brahmaputra-Meghna RB (Fig. 7e–f). The magnitude of seasonal rainfall changes given in Table 5 shows decreasing rainfall in all the seasons over both the river basins especially in winter by most of the datasets including reanalysis products. Consistent with the spatial patterns (Fig. 7), MERRA and CFSR show anomalously large increasing trends during summer in the Brahmaputra-Meghna RB from 1980-2010 (Table 5). Precipitation changes in reanalyses depend on model parameterizations (e.g., convection scheme, moisture transport) and quality of assimilated observations and is also one of the most difficult physical processes to model. Instrumental changes and changing mix of observations might affect the precipitation fields by introducing spurious jumps. Another important factor to be considered is the models ability to simulate the weakening Indian monsoon circulation (*Ramanathan et al.*, 2005; *Chung and Ramanathan*, 2006) and the affects of ENSO and IOD on the rainfall trends. The reliability of reanalyses to

some extent, are seasonally dependent as shown in Table 5.

[TABLE 5 AROUND HERE.]

Observed changes in temperature based on CRU_TS3.22 and UDEL (Fig. 8a–b) show significant warming over majority of the GBM basin with intense warming (up to 0.6°C/decade) over northern Brahmaputra RB (southern Tibet). The warming patterns are very similar between CRU_TS3.22 and UDEL but the later did not show any significant warming over Bangladesh. The warming trends in the northern parts of GBM RB are well captured by the reanalysis products, even though their magnitudes differ considerably over the region (Fig. 8c–e). In reanalyses, temperature is still closely related to the model parameterizations and model uncertainty may play some role in the representation of climate variability in reanalyses. Representation of temperature in reanalyses generally appears more robust than precipitation, likely due to direct assimilation of near surface temperature data from both radiosonde and satellite sources. However, ERA-Interim barely shows any significant warming over the region (Fig. 8c) despite their use of both near surface atmospheric temperature and water vapour to constrain soil moisture (*Dee et al.*, 2011).

MERRA and CFSR (Fig. 8d–e) indicate few areas of negative spurious trends in the northern Brahmaputra (western Ganges) RB. CFSR also uses precipitation observations over land to better constrain their soil moisture (*Saha et al.*, 2010). The excessive warming seen in CFSR over the Himalayan region (Fig. 8e) correlates well with the precipitation increases indicating that warming in this region may be caused by other changes such as limited water storage capacity in the coupled land model. The basin-averaged trends are estimated for all the four seasons and are given in Table 6. Consistent with the spatial patterns observed in Fig. 8, the basin-averaged seasonal trends based on CRU_TS3.22 and UDEL also indicates significant warming in both the river basins during the spring, autumn, and winter. CRU_TS3.22 also showed significant warming trends (0.21°C/dec) in the Brahmaputra-Meghna RB during summer. ERA-Interim was not able to reproduce these seasonal temperature trends,

but MERRA and CFSR agreed well with observed data in the Brahmaputra-Meghna RB (Table 6). Note that all the reanalysis products indicate negative (although not significant) temperature trends in summer over the Ganges RB.

[FIGURE 8 AROUND HERE.]

[TABLE 6 AROUND HERE.]

4.2. Interannual variability of precipitation and temperature

The interannual variability of temperature and precipitation over the GBM basin was examined by applying PCA on the deseasonalized (annual and semi-annual components removed) and detrended (linear trend removed) anomalies of various products for the period 1980 to 2010. PCA was applied to the monthly anomalies (annual signals removed) of CRU_TS3.22 to derive the EOFs (spatial patterns) and PCs (temporal patterns), while the rest of the datasets were projected onto these EOFs to produce their temporal patterns. Only the first two leading modes are considered here due to their distinguished variance contribution. Figure 9 shows the PCA modes of CRU_TS3.22 temperature data together with the projected temporal components of UDEL and the three reanalysis temperature fields. The first orthogonal mode explains about 43% of the variance indicating strong positive anomalies over the western GBM RB and northern Brahmaputra basin (Fig. 9a). The second EOF (with a variance of 13%, Fig. 9b) shows positive (negative) anomalies over Ganges (Brahmaputra-Meghna) RB and strong positive (negative) anomalies over central India (western Tibet).

[FIGURE 9 AROUND HERE.]

The first PC (Fig. 9c) shows considerable interannual variability, indicating the extreme warm (e.g., 1988, 1999) and cold (e.g., 1997–1998, 2008–2009) episodes between 1998 and 2010. The patterns are quite similar in the second PC (Fig. 9d) but tend to differ during the periods 1982–1984 and 1996–2000. UDEL agrees very well with CRU_TS3.22 with a correlation of 0.95 and 0.90 for PC 1 and PC 2, respectively (Table 7). The temporal patterns are captured

very well by the reanalysis products (Fig. 9c–d), especially with ERA-Interim and MERRA showing high correlations with CRU_TS3.22 (Table 7). The correlations between CRU_TS.22 and MERRA for PC 2 is found to be higher (0.79) than those with ERA-Interim (0.68) whereas CFSR agrees only moderately for both the PCs.

[TABLE 7 AROUND HERE.]

In order to examine the mechanisms for these interannual variations, the two PCs (Fig. 9c–d) are correlated with the SST anomalies (50°N–50°S) for the period 1980 to 2010. It must be mentioned here that several studies have attempted to understand the role of SST variations on temperature, but were only focussed on the Indian sub-continent (*Hingane et al.*, 1985; *Kothawale et al.*, 2010; *Chowdary et al.*, 2014). Figure 10 shows the correlation between the two PCs (Fig. 9c-d) and the SST anomalies (50°N–50°S). The two PCs are correlated with each grid element of the SST dataset to generate a temporal correlation as shown in Fig. 10. EOF 1 appears to be highly correlated with SST anomalies over the Arabian Sea, moderately correlated with SST anomalies over Bay of Bengal and the western tropical Pacific Ocean, and negatively correlated with SST over the western Pacific Ocean (Fig. 10a and c). This suggests that warm temperatures in the western Ganges basin are likely driven by local (i.e., Arabic Sea), and remote forcings such as weak La Niña-type events arising from warmer SSTs in the western tropical Pacific Ocean. EOF 2, on the other hand, is found to be highly correlated with SST anomalies in the western tropical Indian Ocean and the western tropical Pacific Ocean. The correlation patterns over the tropical Indian Ocean are similar to that of the IOD (*Saji et al.*, 1999) and those over western tropical Pacific Ocean resemble the El Niño pattern indicating that both ENSO and IOD play a significant role in surface temperature variability across the GBM RB. Their effects are positive (negative) in the Ganges (Brahmaputra-Meghna) RB.

These correlation patterns are very weak in the reanalysis products with only MERRA (and to some extent ERA-Interim) being able to capture the spatial

patterns (Fig. 10e–h). Even though PC 1 of MERRA shows positive correlation over western tropical Pacific Ocean (Fig. 10e), their magnitudes are relatively closer to CRU_TS3.22 than ERA-Interim (Fig. 10g–h) and CFSR (Fig. 10i–j). To quantify the relation between surface temperature and the remote SSTs, PC 2 (Fig. 9c) is correlated with Niño3.4 and DMI indices (Table 8). The correlation between PC 2 and Niño3.4 (DMI) is found to be 0.55 (0.23) based on observed CRU_TS3.22 data and statistically significant at 5% significance level. Correlation with Niño3.4 index is higher for MERRA, followed by ERA-Interim and CFSR, which is found to be consistent with the spatial correlation patterns shown in Fig. 10. However, it is observed that CFSR temperature product is better correlated with DMI than those of MERRA and ERA-Interim. This results shown here are quite interesting because ERA-Interim, albeit having consistent temporal anomalies with respect to CRU_TS3.22 indicates lower correlations with SSTs. This may lead to biases in seasonal precipitation amounts during major ENSO and IOD episodes.

[TABLE 8 AROUND HERE.]

To quantify the impact of ENSO and IOD on the rainfall variations over the GBM RB, the normalized ENSO/IOD indices (Niño3.4 and DMI) are fitted to the rainfall anomalies (annual signals removed) of APHRODITE (1998–2007), TMPAv7 (1998–2013), GPCCv6 (1980–2010), and the reanalysis products (1980–2010). The significance of the regression estimates are tested using a student's t-test at 95% confidence level based on the correlations between Niño3.4/DMI indices and rainfall anomalies at each grid. Correlations between Niño3.4 (and DMI) and rainfall anomalies are found to be significant over few regions with values of up to 0.4 for Niño3.4 (and 0.3 for DMI). Figure 11 shows the rainfall contribution of ENSO and IOD on the total annual rainfall. In general, the positive ENSO mode (or El Niño) is associated with significant reduction of rainfall ($\sim$15 mm/yr) mainly over the western Ganges RB (including southern Nepal, Uttar Pradesh, Bihar, Meghalaya in India and southwest of Bhutan).

While the ENSO impacts are mainly concentrated over western Nepal and its surroundings from 1980 to 2007 (Fig. 11a), the period of 1998–2013 saw widespread reduction of rainfall in the Ganges and northern Brahmaputra RBs (Fig. 11b). However, a slight increase (∼5–10 mm/yr) in rainfall can be seen over Bangladesh during the same period. The IOD mode (Fig. 11c–d), on the other hand is associated with increase (decrease) in rainfall in the southeastern parts of Ganges RB (Bangladesh and Meghalaya in India). During the same period, widespread decreases in rainfall are observed over Bangladesh, which are likely associated with frequent positive IOD events during the period (Fig. 11d). Overall, the influence of ENSO is found to be more dominant (∼10–20% of total rainfall) than the IOD phenomenon (∼8–10%). These estimates were obtained by dividing the ENSO and IOD amplitudes by root-mean-squares of the total rainfall (see e.g., *Forootan et al.*, 2015).

[FIGURE 11 AROUND HERE.]

The influence of ENSO and IOD on precipitation between 1980 and 2010 shown by GPCCv6 (Fig. 12a and e) are found to be consistent with those indicated in APHRODITE from 1980–2007 (Fig. 11a and c), but with a slightly higher precipitation contribution in GPCCv6. This could be due to the more frequent events of La Niña (e.g., in 2007–2008) and El Niño (e.g., in 2006 and 2009–2010) events towards the end of 2010 (see, *Khandu et al.*, 2016b). Among the reanalysis products, ERA-Interim shows the closest agreement with gauge-based precipitation product, GPCCv6 (Fig. 12b and f) whereas MERRA (Fig. 12c and g) and CFSR (Fig. 12d and h) either underestimate or overestimate rainfall contribution due to ENSO and IOD events. However, it should be noted that the spatial patterns of ENSO and IOD contributions are captured reasonably well by all the products.

[FIGURE 12 AROUND HERE.]

5. Conclusion

This study examined the seasonal and interannual variability of rainfall and temperature over the GBM RB using available observational gauge-, SRS-based, and global high-resolution reanalysis products covering the period 1980–2013. The reanalysis systems in particular, provide long time-series of climate datasets that are important for understanding various aspects of global/regional climate variability and change. They also act as reference climate forcing data for regional climate and hydrological modelling. The trend results indicate widespread warming across the GBM RB during the last 30 years. Warming appears to be more intense over the northern parts of the basin (western Nepal and Tibetan region) than the southern (e.g., Bangladesh) and western parts of the GBM RB with a maximum increase in temperature of 0.6°C/decade over the northern Brahmaputra RB (southern Tibet). Rainfall changes over various periods between 1980 and 2013 indicate significant decline over the GBM RB. In particular, SRS-based precipitation products such as TMPAv7 and CHIRP reveal pronounced monsoon rainfall decline over the last 15 years (from 1998–2013) in the high rainfall regions of northeast India, southwest Bhutan, Nepal, and Bangladesh (39 mm/decade during June-August). However, the monsoon rainfall appears to be increasing in the Ganges RB between 1998 and 2013 at a rate of 12 mm/decade, but are found to be insignificant.

In terms of the interannual variations, temperature variations can be summarized in the first two orthogonal modes of PCA, which accounts for ∼56% of the total variability. The first EOF shows basin-wide positive anomalies with increasing magnitudes towards the west and north and are associated with warming SSTS over the Arabic Sea and the western tropical Pacific Ocean. The second EOF indicates a dipole-type pattern with positive (negative) anomalies over Ganges (Brahmaputra-Meghna) RBs and are significantly correlated to SST anomalies over western tropical Indian Ocean and eastern tropical Pacific Ocean. Thus, it is observed that surface temperature variations over the basin are both influenced by local (e.g., Arabic Sea) and remote (e.g., ENSO

and IOD) SST variations. Similarly, ENSO and IOD events are found to have significant influences on the seasonal rainfall across the GBM RB. The contribution of ENSO and IOD to the total annual rainfall is about 10–20% and 8–10%, respectively, affecting rainfalls mainly over southwest Bhutan, Nepal, northern Bangladesh, and northern parts of India (e.g., Bihar, Uttar Bangladesh, West Bengal, and Meghalaya).

The quality of the reanalysis products are found to be relatively poor over the GBM RB compared to the observed gauge-based datasets. It should be mentioned here that no single reanalysis is superior to others for both rainfall and temperature in reproducing the changes and variability. Among the reanalysis products examined in this study, MERRA temperature data is found to agree well with CRU_TS3.22, while ERA-Interim is closer to GPCCv6 precipitation data in terms of trends and interannual variability. MERRA and ERA-Interim products are able to barely capture the spatial precipitation variability across the GBM RB during the monsoon, while CFSR tends to shift the high rainfall regions e.g., southwest of Bhutan, to the east. The annual amplitudes of MERRA precipitation fields is found to be significantly lower (by about 21–37%) compared to the GPCCv6 data, while CFSR overestimated it by about 9%. Despite showing considerable biases in precipitation and temperature, these products are able to represent the spatial patterns of ENSO and IOD contributions on precipitation.

Acknowledgements

Khandu is grateful to Curtin Strategic International Research Scholarship, Curtin University (Australia) for the financial support. He also acknowledges the financial support of Prince Albert II of Monaco Foundation and the Intergovernmental Panel on Climate Change (IPCC). J. L. Awange acknowledges the financial support from Brazilian Science Without Borders Program/CAPES Grant No. 88881.068057/2014-01 in collaboration with the Federal University of Pernambuco (UFPE, Brazil). Further, the authors are grateful to APHRODITE,

Climate Research Unit (CRU), Global Precipitation Climatology Centre (GPCC), National Aeronautics and Space Administration (NASA), the Climate Prediction Center (CPC), and the European Centre for Medium-Range Weather Forecasts (ECMWF) for providing the necessary datasets used in this study.

Appendix A1. Trend estimation

For illustration purposes, let us consider a matrix $\mathbf{X}_{n\times m}$, containing the time-series of monthly rainfall (or temperature) over the GBM RB, after removing their long-term temporal mean, where n describes the time (in months) and m represents the spatial locations (as stations or grids).

(i) **Multiple linear regression (MLR)**: The MLR model can be formulated to characterize trends and seasonality in the dataset:

$$\mathbf{X} = x(j) = \beta_0 + \beta_1(j).t + \beta_2(j).\cos(2\pi t) + \beta_3(j).\sin(2\pi t) + \beta_4(j).\cos(4\pi t) + \beta_5(j).\sin(4\pi t) + \epsilon(t), \quad (1)$$

where β_0-β_5 are the coefficients of MLR for $j = 1, ..., m$, and ϵ are the residuals. The coefficients $\beta_{1...5}(j)$ are estimated by the least squares adjustment method and represents the terms linear trends (β_1), mean annual variability (β_2, β_3), and semi-annual variability (β_4, β_5). The inter-annual variability ($\hat{\mathbf{X}}$) is usually related to large-scale ocean-atmospheric phenomenon such as ENSO and IOD modes, among others, and can be formulated as:

$$\hat{\mathbf{X}} = \hat{x}(j) - \Big[\hat{\beta}_1(j).t + \hat{\beta}_2(j).\cos(2\pi t) + \hat{\beta}_3(j).\sin(2\pi t) + \hat{\beta}_4(j).\cos(4\pi t) + \hat{\beta}_5(j).\sin(4\pi t)\Big], \quad (2)$$

(ii) **Sen's slope estimation**: The least squares estimation of regression coefficient $\hat{\beta}_1$ is vulnerable to gross errors and sensitive to non-normality of the probability distribution. *Sen* (1968)'s slope estimator is a common approach for assessing trends in hydrological time-series (e.g., precipitation)

as it is less sensitive to outliers. In this method, the slopes (T_i) of all data pairs in time are first calculated by

$$T_i = \frac{x_k - x_l}{k - l} \quad \text{for } i = 1, 2, ...n, \tag{3}$$

where x_k and x_l are data values at time k and l ($k > l$), respectively. The median values of these n values of T_i is the Sen's slope ($\hat{\beta}$), which is calculated as:

$$\hat{\beta} = \begin{cases} T_{\frac{n+1}{2}} & n \text{ is odd} \\ \frac{1}{2}\left(T_{\frac{n}{2}} + T_{\frac{n+2}{2}}\right) & n \text{ is even} \end{cases} \tag{4}$$

where β can be both positive (increasing trend) or negative (decreasing trend).

Appendix A2. Significance testing

The significance of linear trends estimated above should be tested by determining whether the derived trends in rainfall and temperature are significantly different from zero. Typically, the null hypothesis is H_0: $\beta_1 = 0$ (no trend), while the alternative hypothesis, H_1: $\beta_1 \neq 0$ (trend). Two approaches were used in this study and are briefly described below:

(i) **Mann-Kendall Test**: The Mann-Kendall test (*Mann*, 1945; *Kendall*, 1962) is a non-parametric approach, which searches for a trend in time-series without specifying whether the trend is linear or non-linear. The test statistics (S) is defined as:

$$S = \sum_{i=1}^{n-1} \sum_{j=i+1}^{n} \text{sgn}(x_j - x_i), \tag{1}$$

where n is the number of data points. Assuming $(x_j - x_i)$=θ, the value of sgn(θ) is calculated as:

$$\text{sgn}(\theta) = \begin{cases} 1 & \text{if } \theta > 0 \\ 0 & \text{if } \theta = 0 \\ -1 & \text{if } \theta < 0 \end{cases} \tag{2}$$

S represents the sum of positive and negative changes for all the data pairs and for samples ($n > 10$), the test is conducted using a normal distribution with mean, variance, and test value of:

$$E[S] = 0$$

$$\mathrm{Var}[S] = \frac{n(n-1)(2n+5) - \sum_{k=1}^{n} t_k(t_k-1)(2t_k+5)}{18}, \tag{3}$$

$$Z = \begin{cases} \frac{S-1}{\sqrt{\mathrm{Var}(S)}} & \text{if } S > 0 \\ 0 & \text{if } S = 0 \\ \frac{S+1}{\sqrt{\mathrm{Var}(S)}} & \text{if } S < 0 \end{cases} \tag{4}$$

If $|Z| > z_{\alpha/2}$ (where $\alpha/2$ indicates the quantile of the normal distribution), the null hypothesis (no trend, denoted by H_0) is rejected at α significance level (at 5%) in a two sided test. For seasonal and annual time-series, it is also important to take into account the autocorrelation structure (or serial correlation) in the data. Autocorrelation increases the probability of detecting significant trends. *Hamed and Rao* (1998) suggested a modified Mann-Kendall approach by considering the autocorrelation between the ranks of the data. This is done by modifying the variance, Here, the modified Mann-Kendall test was used and the null hypothesis was tested at 95% confidence level.

(ii) **Student *t-test***: Students *t-test* is one of the widely used method for determining whether the trend is statistically significant. For example, consider a time-series of rainfall anomalies ($x(t)$) with an estimated linear trend of $\hat{\beta}_1$, it's residuals ($\epsilon(t)$) can be derived as difference of observed rainfall anomalies ($x(t)$) and those estimated from e.g., MLR model ($\hat{x}(t)$) over $t = 1, 2, ..., n$ months:

$$\epsilon(t) = x(t) - \hat{x}(t), \tag{5}$$

and the standard error (S_β) of $\hat{\beta}_1$ is defined as

$$S_\beta = \frac{S_\epsilon}{\sqrt{\sum_{t=1}^{n}(t-\bar{t})^2}}, \tag{6}$$

where S_ϵ^2, variance of the residuals (ϵ) is given by

$$S_\epsilon^2 = \frac{1}{n-2}\sum_{t=1}^{n}\epsilon(t)^2, \tag{7}$$

In order to examine whether the trend in $x(t)$ is significantly different from 0, a test value is computed as a ratio between the estimated trend ($\hat{\beta}_1$) and its standard error (S_β):

$$t_\beta = \frac{\hat{\beta}_1}{S_\beta} \tag{8}$$

assuming that t_β follows a t-distribution. The null hypothesis (no trend or H_0 is rejected if $|t| < t_{\text{crit}}$, where t_{crit} is the point on the student's t-distribution with $n-2$ degrees of freedom. It should be noted that while the t-test is simple and powerful to normally distributed data (e.g., temperature), it is less powerful against non-normally distributed data (e.g., monthly rainfall).

Appendix A3. Principal Component Analysis (PCA)

The central idea of the PCA analysis is to find a set of orthogonal spatial patterns (Empirical Orthogonal Functions or EOFs) along with a set of associated uncorrelated time-series or principal components (PCs) that captures most of the observed variance (expressed in %) from the available spatio-temporal data such as precipitation and temperature. In summary, the EOF decomposition can be written as $\mathbf{X}_{(n,m)} \cong \mathbf{P}_{(n,k)}\mathbf{E}^{\mathrm{T}}_{(m,k)}$ where $\mathbf{X}_{(n,m)}$ is the time (n)-space (m) data (e.g., precipitation), $\mathbf{E}_{(m,k)}$ contains the EOFs with k number of retained modes, and $\mathbf{P}_{(n,k)}$ are the PCs obtained by projecting the original data ($\mathbf{X}_{(n,m)}$) on the orthogonal base-functions $\mathbf{E}_{(m,k)}$, i.e., $\mathbf{P}_{(n,k)} = \mathbf{X}_{(n,m)}\mathbf{E}_{(m,k)}$. This method can be applied at various stages of the analysis in order to find any meaningful links to various dynamics of the climate system using a subset of PCs.

References

Andermann, C., S. Bonnet, and R. Gloaguen (2011), Evaluation of precipitation data sets along the Himalayan front, *Geochemistry, Geophysics, Geosystems*, *7*(12), doi:10.1029/2011GC003513.

Balsamo, G., C. Albergel, A. Beljaars, S. Boussetta, E. Brun, H. Cloke, D. Dee, E. Dutra, J. Muñoz-Sabater, F. Pappenberger, P. de Rosnay, T. Stockdale, and F. Vitart (2015), ERA-Interim/Land: A global land surface reanalysis data set, *Hydrol. Earth Syst. Sci.*, *19*, 389–407, doi:10.5194/hess-19-389-2015.

Barros, A. P., G. Kim, E. Williams, and S. W. Nesbitt (2004), Probing orographic controls in the Himalayas during the monsoon using satellite imagery, *Nat. Hazards Earth Syst. Sci.*, *4*(1), 29–51, doi:10.5194/nhess-4-29-2004.

Chowdary, J. S., N. John, and C. Gnanaseelan (2014), Interannual variability of surface air-temperature over India: impact of ENSO and Indian Ocean sea surface temperature, *Int. J. Climatol.*, *34*(2), 416–429, doi:10.1002/joc.3695.

Chowdhury, M. D. R., and N. Ward (2004), Hydro-meteorological variability in the greater Ganges-Brahmaputra-Meghna basins, *Int. J. Climatol.*, *24*(12), 1495–1508, doi:10.1002/joc.1076.

Chung, C. E., and V. Ramanathan (2006), Weakening of North Indian SST gradients and the monsoon rainfall in India and the Sahel, *J. Clim.*, *19*, 2036–2045, doi:10.1175/JCLI3820.1.

Dee, D. P., S. M. Uppala, A. J. Simmons, P. Berrisford, P. Poli, S. Kobayashi, U. Andrae, M. A. Balmaseda, , G. Balsamo, P. Bauer, P. Bechtold, A. C. M. Beljaars, L. van de Berg, J. Bidlot, N. Bormann, C. Delsol, R. Dragani, M. Fuentes, A. J. Geer, L. Haimbergere, S. B. Healy, H. Hersbach, E. V. Holm, L. Isaksen, P. Kållberg, M. Köhler, M. Matricardi, A. P. McNally, B. M. Monge-Sanz, J.-J. Morcrette, B.-K. Park, C. Peubey, P. de Rosnay, C. Tavolato, J.-N. Thépaut, and F. Vitarta (2011), The ERA-Interim reanal-

ysis: Configuration and performance of the data assimilation system, *Q. J. R. Meteorolog. Soc.*, *137*, 553–597, doi:10.1002/qj.828.

Dimri, A. P., D. Niyogi, A. P. Barros, J. Ridley, U. C. Mohanty, T. Yasunari, and D. R. Sikka (2015), Western Disturbances: A Review, *Rev. Geophys.*, *53*(2), 225–246, doi:10.1002/2014RG000460.

Duncan, J. M., and E. M. Biggs (2012), Assessing the accuracy and applied use of satellite-derived precipitation estimates over Nepal, *Appl. Geogr.*, *34*, 626–638, doi:10.1016/j.apgeog.2012.04.001.

FAO (2011), Ganges-brahmaputra-meghna basin, *Tech. Rep. Water Report 37*, AQUASTAT, Food and Agriculture Organization of the United Nations, Rome, Italy, available from: http://www.fao.org/nr/water/aquastat/basins/gbm/index.stm. Accessed on 21 Feb 2015.

Flato, G., J. Marotzke, B. Abiodun, P. Braconnot, S. Chou, W. Collins, P. Cox, F. Driouech, S. Emori, V. Eyring, C. Forest, P. Gleckler, E. Guilyardi, C. Jakob, V. Kattsov, C. Reason, and M. Rummukainen (2013), Evaluation of climate, in *Climate Change 2013: The Physical Science Basis. Contribution of Working Group I to the Fifth Assessment Report of the Intergovernmental Panel on Climate Change*, edited by T. F. Stocker, D. Qin, G.-K. Plattner, M. Tignor, S. Allen, J. Boschung, A. Nauels, Y. Xia, V. Bex, and P. Midgley, Cambridge University Press, Cambridge, United Kingdom and New York, NY, USA.

Forootan, E. (2014), Statistical Signal Decomposition Techniques for Analyzing Time-Variable Satellite Gravimetry Data, Ph.D. thesis, Universität Bonn, Bonn, Germany.

Forootan, E., Khandu, J. L. Awange, M. Schumacher, R. Anyah, A. van Dijk, and J. Kusche (2015), Quantifying the impacts of ENSO and IOD on rain gauge and remotely sensed precipitation products over Australia, *Remote Sens. Environ.*, *172*, 50–66, doi:10.1016/j.rse.2015.10.027.

804 Forsythe, N., S. Blenkinsop, and H. J. . Fowler (2014), Exploring objective
805 climate classification for the Himalayan arc and adjacent regions using gridded
806 data sources, *Earth Syst. Dynam.*, *6*, 311–326, doi:10.5194/esd-6-311-2015.

807 Funk, C., J. Michaelsen, and M. T. Marshall (2012), Mapping recent decadal
808 climate variations in precipitation and temperature across eastern africa and
809 the sahel, in *Remote Sensing of Drought: Innovative Monitoring Approaches*,
810 edited by B. D. . Wardlow, M. C. . Anderson, and J. P. Verdin, chap. 14, pp.
811 331–357, CRC Press 2012.

812 Funk, C. C., P. J. Peterson, M. F. Landsfeld, D. H. Pedreros, J. P. Verdin, J. D.
813 Rowland, B. E. Romero, G. J. Husak, J. C. Michaelsen, and A. P. Verdin
814 (2014), A quasi-global precipitation time series for drought monitoring, *U.S.*
815 *Geol. Surv. Data Ser.*, *27*, 1062–1069, doi:10.1175/JCLI-D-13-00332.1.

816 Hamed, K. H., and A. R. Rao (1998), A modified Mann-Kendall trend
817 test for autocorrelated data, *J. Hydrol.*, *204*(1-4), 182–196, doi:10.1016/
818 S0022-1694(97)00125-X.

819 Hannachi, A., I. T. Jolliffe, and D. B. Stephenson (2007), Empirical orthogonal
820 functions and related techniques in atmospheric science: A review, *Int. J.*
821 *Climatol.*, *27*(9), 1119–1152, doi:10.1002/joc.1499.

822 Harris, I., P. Jones, T. Osborn, and D. Lister (2013), Updated high-resolution
823 grids of monthly climatic observations- the CRU TS3.10 Dataset, *Int. J. Cli-*
824 *matol.*, *34*(3), 623–642, doi:10.1002/joc.3711.

825 Helsel, D., and R. Hirsch (2002), Statistical methods in water resources, in
826 *Techniques of Water Resources Investigations*, Book 4, chap. A3, p. 522pp,
827 U.S. Geological Survey.

828 Hingane, L. S., K. R. Kumar, and B. V. R. Murty (1985), Long-term trends
829 of surface air temperature in India, *Int. J. Climatol.*, *5*(5), 521–528, doi:
830 10.1002/joc.3370050505.

Hirsch, R. M., and J. R. Slack (1984), A nonparametric trend test for seasonal data with serial dependence, *Water Resour. Res.*, *6*(20), 727–732, doi:10.1029/WR020i006p00727.

Huffman, G. J., and D. T. Bolvin (2013), TRMM and other data precipitation data set documentation, *Tech. rep.*, Mesoscale Atmospheric Processes Laboratory, NASA Goddard Space Flight Center and Science Systems and Applications, Inc.

Huffman, G. J., D. T. Bolvin, E. J. Nelkin, D. B. Wolff, R. F. Adler, G. Gu, Y. Hong, K. P. Bowman, and E. F. Stocker (2007), The TRMM Multisatellite Precipitation Analysis (TMPA): Quasi-Global, Multiyear, Combined-Sensor Precipitation Estimates at Fine Scales, *J. Hydrometeorol.*, *8*(1), 38–55, doi:10.1175/JHM560.1.

Joyce, R. J., J. E. Janowiak, P. A. Arkin, and P. Xie (2004), CMORPH: A method that produces global precipitation estimates from passive microwave and infrared data at high spatial and temporal resolution, *J. Hydrometeorol.*, *5*(3), 487–503, doi:10.1175/1525-7541(2004)005⟨0487:CAMTPG⟩2.0.CO;2.

Kalnay, E., M. Kanamitsu, R. Kistler, W. Collins, D. Deaven, L. Gandin, M. Iredell, S. Saha, G. White, J. Woollen, Y. Zhu, M. Chelliah, W. Ebisuzaki, W. Higgins, J. Janowiak, K. C. Mo, C. Ropelewski, J. Wang, A. Leetmaa, R. Reynolds, R. Jenne, , and D. Joseph (1996), The NCEP/NCAR 40-year reanalysis project, *Bull. Am. Meteorol. Soc.*, *77*(3), 437–470, doi:10.1175/1520-0477(1996)077⟨0437:TNYRP⟩2.0.CO;2.

Kanamitsu, M., W. Ebisuzaki, J. Woollen, S.-K. Yang, J. J. Hnilo, M. Fiorino, and G. L. Potter (2002), NCEP-DOE AMIP-II Reanalysis (R-2), *Bull. Am. Meteorol. Soc.*, *83*, 1631–1643, doi:10.1175/BAMS-83-11-1631.

Kendall, M. G. (1962), Rank correlation methods, *J. Am. Stat. Assoc.*, *63*(324), 1379–1389, doi:10.1080/01621459.1968.10480934.

858 Khandu, J. L. Awange, and E. Forootan (2016a), An evaluation of high-
859 resolution gridded precipitation products over Bhutan (1998-2012), *Int. J.*
860 *Climatol.*, *36*(3), 1067–1087, doi:10.1002/joc.4402.

861 Khandu, E. Forootan, M. Schumacher, J. Awange, and H. M. Schmied (2016b),
862 Exploring the influence of precipitation extremes and human water use on to-
863 tal water storage (tws) changes in Brahmaputra-Ganges-Meghna Basin, *Wa-*
864 *ter Resour. Res.*, doi:10.1002/2015WR018113, accepted.

865 Kishore, P., S. Jyothi, G. Basha, S. V. B. Rao, M. Rajeevan, and I. Velicogna
866 (2016), Precipitation climatology over India: validation with observations
867 and reanalysis datasets and spatial trends, *Clim. Dyn.*, *46*(1), 541–556, doi:
868 10.1007/s00382-015-2597-y.

869 Kobayashi, S., Y. Ota, Y. Harada, A. Ebita, M. Moriya, H. Onoda, K. Onogi,
870 H. Kamahori, C. Kobayashi, H. Endo, K. Miyaoka, and K. Takahashi (2015),
871 The JRA-55 Reanalysis: General specifications and basic characteristics,
872 *Quart. J. R. Meteorol. Soc.*, *93*(1), 5–48, doi:10.2151/jmsj.2015-001.

873 Kothawale, D. R., , A. A. Munot, and K. K. Kumar (2010), Surface air temper-
874 ature variability over India during 1901-2007, and its association with ENSO,
875 *Clim. Res.*, *42*(1), 89–104, doi:10.3354/cr00857.

876 Legates, D. R., and C. J. Willmott (1990), Mean seasonal and spatial variability
877 in global surface air temperature, *Theor. Appl. Climatol.*, *41*(1), 11–21, doi:
878 10.1007/BF00866198.

879 Mann, H. B. (1945), Nonparametric tests against trend, *Econometrica*, *13*(3),
880 245–259.

881 Misra, V., P. Pantina, S. C. Chan, and S. DiNapoli (2012), A comparative
882 study of the Indian summer monsoon hydroclimate and its variations in three
883 reanalyses, *Clim. Dyn.*, *39*(5), 1149–1168, doi:10.1007/s00382-012-1319-y.

884 Onogi, K., H. Koide, M. Sakamoto, S. Kobayashi, J. Tsutsui, H. Hatsushika,
885 T. Matsumoto, N. Yamazaki, H. Kamahori, K. Takahashi, K. Kato, T. Ose,

S. Kadokura, and K. Wada (2005), JRA-2: Japanese 25-year Reanalysis, *Quart. J. R. Meteorol. Soc.*, *131*(613), 3259–3268, doi:10.1256/qj.05.88.

Onogi, K., J. Tsutsui, H. Koide, M. Sakamoto, S. Kobayashi, H. Hatsushika, T. Matsumoto, N. Yamazaki, H. Kamahori, K. Takahashi, S. Kadokura, K. Wada, K. Kato, R. Oyama, T. Ose, N. Mannoji, and R. Taira (2007), The JRA-25 Reanalysis, *Quart. J. R. Meteorol. Soc.*, *85*(3), 369–432, doi: 10.2151/jmsj.85.369.

Peña-Arancibia, J. L., A. I. J. M. van Dijk, L. J. Renzullo, and M. Mulligan (2013), Evaluation of precipitation estimation accuracy in reanalyses, satellite products, and an ensemble method for regions in Australia and South and East Asia, *J. Hydrometeor*, *4*(14), 13231333, doi:10.1175/JHM-D-12-0132.1.

Prakash, S., V. Sathiyamoorthy, C. Mahesh, and R. M. Gairola (2014), An evaluation of high-resolution multisatellite rainfall products over the Indian monsoon region, *Int. J. Remote Sens.*, *35*(9), 3018–3035, doi:10.1080/01431161.2014.894661.

Prakash, S., A. K. Mitra, I. M. Momin, E. N. Rajagopal, S. Basu, M. Collins, A. G. Turner, K. A. Rao, and K. Ashok (2015), Seasonal intercomparison of observational rainfall datasets over india during the southwest monsoon season, *Int. J. Remote Sens.*, *35*(9), 2326–2338, doi:10.1002/joc.4129.

Preisendorfer, R. W. (1988), *Principal component analysis in meteorology and oceanography*, 425 pp., Elsevier.

Rajeevan, M., and J. Bhate (2008), A high resolution daily gridded rainfall data set (1971-2005) for mesoscale meteorological studies, *Tech. Rep. NCC Research Report No. 9*, National Climate Centre, Indian Meteorological Department, Pune, India, available from http://www.imdpune.gov.in/ncc_rept/RESEARCH%20REPORT%209.pdf, accessed on: 21 June 2014.

Rajeevan, M., and J. Bhate (2009), A high resolution daily gridded rainfall

dataset (1971-2005) for mesoscale meteorological studies, *Curr. Sci.*, *96*, 558–562.

Ramanathan, V., C. Chung, D. Kim, T. Bettge, L. Buja, J. T. Kiehl, W. M. Washington, Q. Fu, D. R. Sikka, , and M. Wild (2005), Atmospheric brown clouds: Impacts on South Asian climate and hydrological cycle, *Proc. Natl. Acad. Sci. U.S.A*, *102*(15), 5326–5333, doi:10.1073pnas.0500656102.

Rayner, N. A., D. E. Parker, E. B. Horton, C. K. Folland, L. V. Alexander, D. P. Rowell, E. C. Kent, and A. Kaplan (2003), Global reanalyses of sea surface temperature, sea ice, and night marine air temperature since the late nineteenth century, *J. Geophys. Res.*, *108*(D14), doi:10.1029/2002JD002670.

Rienecker, M. M., M. J. Suarez, R. Gelaro, R. Todling, J. Bacmeister, E. Liu, M. G. Bosilovich, S. D. Schubert, L. Takacs, G. K. Kim, S. Bloom, J. Chen, D. Collins, A. Conaty, A. da Silva, W. Gu, J. Joiner, R. D. Koster, R. Lucchesi, A. Molod, T. Owens, S. Pawson, P. Pegion, C. R. Redder, R. Reichle, F. R. Robertson, A. G. Ruddick, M. Sienkiewicz, and J. Woollen (2011), MERRA: NASA's Modern-Era Retrospective Analysis for Research and Applications, *J. Clim.*, *24*(14), 3624–3648, doi:10.1175/JCLI-D-11-00015.1.

Saha, S., S. Moorthi, H.-L. Pan, X. Wu, J. Wang, S. Nadiga, P. Tripp, R. Kistler, J. Woollen, D. Behringer, H. Liu, D. Stokes, R. Grumbine, G. Gayno, J. Wang, Y. T. Hou, H. Y. Chuang, H.-M. H. Juang, J. Sela, M. Iredell, R. Treadon, D. Kleist, P. V. Delst, D. Keyser, J. Derber, M. Ek, J. Meng, H. Wei, R. Yang, S. Lord, H. V. D. Dool, A. Kumar, W. Wang, C. Long, M. Chelliah, Y. Xue, B. Huang, J.-K. Schemm, W. Ebisuzaki, R. Lin, P. Xie, M. Chen, S. Zhou, W. Higgins, C.-Z. Zou, Q. Liu, Y. Chen, Y. Han, L. Cucurull, R. W. Reynolds, G. Rutledge, and M. Goldberg (2010), The NCEP Climate Forecast System Reanalysis, *Bull. Am. Meteorol. Soc.*, *91*(8), 1015–1057, doi:10.1175/2010BAMS3001.1.

Saji, N. H., B. N. Goswami, P. N. Vinayachandran, and T. Yamagata (1999), A dipole mode in the tropical Indian Ocean, *Nature*, *401*, 360–363.

Schneider, U., A. Becker, P. Finger, A. M.-. Christoffer, M. Ziese, and B. Rudolf (2014), GPCC's new land surface precipitation climatology based on quality-controlled in situ data and its role in quantifying the global water cycle, *Theor. Appl. Climatol.*, *115*(1-2), 15–40, doi:10.1007/s00704-013-0860-x.

Sen, P. K. (1968), Estimates of the regression coefficient based on Kendall's Tau, *J. Am. Stat. Assoc.*, *63*(324), 1379–1389, doi:10.1080/01621459.1968.10480934.

Shah, R., and V. Mishra (2014), Evaluation of the reanalysis products for the monsoon season droughts in India, *J. Hydrometeor*, *15*(4), 1575–1591, doi:10.1175/JHM-D-13-0103.1.

Shrestha, D., P. Singh, and K. Nakamura (2012), Spatiotemporal variation of rainfall over the central Himalayan region revealed by TRMM Precipitation Radar, *J. Geophys. Res.*, *117*(D22), doi:10.1029/2012JD018140.

Sorooshian, S., K. Hsu, X. Gao, H. Gupta, B. Imam, and D. Braithwaitea (2000), Evaluation of PERSIANN System Satellite-Based Estimates of tropical rainfall, *Bull. Am. Meteorol. Soc.*, *81*(9), 2035–2046.

Steckler, M. S., S. L. Nooner, S. H. Akhter, S. K. Chowdhury, S. Bettadpur, L. Seeber, and M. G. Kogan (2010), Modeling Earth deformation from monsoonal flooding in Bangladesh using hydrographic, GPS, and Gravity Recovery and Climate Experiment (GRACE) data, *J. Geophys. Res.*, *15*(B8), doi:10.1029/2009JB007018.

Trenberth, K. E. (1990), Recent observed interdecadal climate changes in the Northern Hemisphere, *Bull. Amer. Meteor. Soc.*, *71*(7), 988993, doi:10.1175/1520-0477(1990)071⟨0988:ROICCI⟩2.0.CO;2.

Turk, F. J., and S. D. Miller (2005), Toward improved characterization of remotely sensed precipitation regimes with MODIS/AMSR-E blended data techniques, *IEEE Trans. Geosci. Remote Sens.*, *43*(5), 1059–1069, doi:10.1109/TGRS.2004.841627.

970 Uppala, S. M., P. W. KÅllberg, A. J. Simmons, U. Andrae, V. D. C. Bech-
971 told, M. Fiorino, J. K. Gibson, J. Haseler, A. Hernandez, G. A. Kelly,
972 X. Li, K. Onogi, S. Saarinen, N. Sokka, R. P. Allan, E. Andersson, K. Arpe,
973 M. A. Balmaseda, A. C. M. Beljaars, L. V. D. Berg, J. Bidlot, N. Bormann,
974 S. Caires, F. Chevallier, A. Dethof, M. Dragosavac, M. Fisher, M. Fuentes,
975 S. Hagemann, E. Hólm, B. J. Hoskins, L. Isaksen, P. A. E. M. Janssen,
976 R. Jenne, A. P. Mcnally, J.-F. Mahfouf, J.-J. Morcrette, N. A. Rayner, R. W.
977 Saunders, P. Simon, A. Sterl, K. E. Trenberth, A. Untch, D. Vasiljevic,
978 P. Viterbo, and J. Woollen (2005), The ERA-40 re-analysis, *Q. J. R. Me-*
979 *teorolog. Soc.*, *131*, 2961–3012, doi:10.1256/qj.04.176.

980 Ushio, T., K. Sasashige, T. Kubota, S. Shige, K. Okamoto, K. Aonashi, T. In-
981 oue, N. Takahashi, and T. Iguchi (2009), A kalman filter approach to the
982 Global Satellite Mapping of Precipitation (GSMaP) from combined passive
983 microwave and infrared radiometric data, *J. Meteor. Soc. Japan*, *87A*(9),
984 3084–3097, doi:10.2151/jmsj.87A.137.

985 Willmott, C. J., and S. M. Robeson (1995), Climatologically aided interpolation
986 (CAI) of terrestrial air temperature, *Int. J. Climatol.*, *15*(2), 221–229, doi:
987 10.1002/joc.3370150207.

988 Xie, P., Y. Yarosh, T. Love, J. E. Janowiak, and P. A. Arkin (2002), A real-
989 time daily precipitation analysis over south asia, in *16th Conference of Hy-*
990 *drology*, NOAA/Climate Prediction Center, American Meteorological Society,
991 Orlando, Florida, available at: http://www.cpc.ncep.noaa.gov/products/
992 fews/sasia_rfe.pdf.

993 Xie, P., M. Chen, S. Yang, A. Yatagai, T. Hayasaka, Y. Fukushima, and C. Liu
994 (2007), A gauge-based analysis of daily precipitation over East Asia, *J. Hy-*
995 *drometeorol.*, *8*(3), 607–626, doi:10.1175/JHM583.1.

996 Xue, X., Y. Hong, A. S. Limaye, J. J. Gourley, G. J. Huffman, S. I. Khan,
997 C. Dorji, and S. Chen (2013), Statistical and hydrological evaluation of
998 TRMM-based Multi-satellite Precipitation Analysis over the Wangchu Basin

of Bhutan: Are the latest satellite precipitation products 3b42v7 ready for use in ungauged basins?, *J. Hydrol.*, *499*, 91–99, doi:10.1016/j.jhydrol.2013.06.042.

Yasutomi, N., A. Hamada, and A. Yatagai (2011), Development of a long-term daily gridded temperature dataset and its application to rain/snow discrimination of daily precipitation, *Global Environ. Res.*, *V15N2*, 165–172.

Yatagai, A., K. Kamiguchi, O. Arakawa, A. Hamada, N. Yasutomi, and A. Kitoh (2012), APHRODITE: Constructing a Long-term Daily Gridded Precipitation Dataset for Asia based on a Dense Network of Rain Gauges, *Bull. Am. Meteorol. Soc.*, *93*, 1401–1415, doi:10.1175/BAMS-D-11-00122.1.

Yin, Z. Y., X. Zhang, X. Liu, M. Colella, and X. Chen (2008), An assessment of the biases of satellite rainfall estimates over the Tibetan Plateau and correction methods based on topographic analysis, *J. Hydrometeor*, *9*, 301–326, doi:10.1175/2007JHM903.1.

Table 1: Details of rain gauge products and near-global high-resolution SRS-based precipitation products that have been regularly applied over various parts of the GBM RB.

Product	Period	Spatial Resl.	Temporal Resl.	Coverage	References
		Rain gauge products			
APHRODITE	1951-2007	0.25° × 0.25°	Daily	Asia	*Yatagai et al.* (2012)
IMD	1971-2005	1.0° × 1.0°	Daily	India	*Rajeevan and Bhate* (2009)
GPCCv6	1901-2010	0.50° × 0.50°	Monthly	Global-land	*Schneider et al.* (2014)
CRU_TS3.23	1901-2014	0.50° × 0.50°	Monthly	Global-land	*Harris et al.* (2013)
CPC	1948-present	0.25° × 0.25°	Daily	Global-land	*Xie et al.* (2007)
		Satellite-based precipitation estimates			
CHIRP	1981-present	0.05° × 0.05°	Weekly	50S-50N	*Funk et al.* (2014)
CMORPH	2003-present	0.25° × 0.25°	3-hourly	50S-50N	*Joyce et al.* (2004)
CPC-RFE	2001-present	0.10° × 0.10°	Daily	South Asia	*Xie et al.* (2002)
GSMaP_MVK	2002-present	0.10° × 0.10°	1-hourly	60S-60N	*Ushio et al.* (2009)
NRL-Blend	2002-present	0.10° × 0.10°	3-hourly	60S-60N	*Turk and Miller* (2005)
PERSIANN	2000-present	0.25° × 0.25°	6-hourly	50S-50N	*Sorooshian et al.* (2000)
TRMM 3B42v6	1998-2010	0.25° × 0.25°	3-hourly	50S-50N	*Huffman et al.* (2007)
TRMM 3B42v7	1998-2014	0.25° x× 0.25°	3-hourly	50S-50N	*Huffman and Bolvin* (2013)

Table 2: List of gridded temperature datasets used in this study. All datasets consist of land surface air temperatures derived from ground-based stations across the region.

Product	Period	Spatial Resl.	Temporal Resol.	Coverage	References
APHRODITE	1951-2007	0.25° × 0.25°	Daily	Asia	*Yasutomi et al.* (2011)
CRU	1901-2013	0.50° × 0.50°	Monthly	Global-land	*Harris et al.* (2013)
UDel	1900-2012	0.50° × 0.50°	Monthly	Global-land	*Willmott and Robeson* (1995)

Table 3: Details of the three reanalyses used in this study. All datasets consist of terrestrial surface air temperatures.

Product	Period	Spatial Resl.	Temporal Resl.	Coverage	References
ERA-Interim Land	1979-2010	0.79° × 0.79°	6-hourly	Global	*Dee et al.* (2011)
MERRA Land	1980-2010	0.67° × 0.50°	6-hourly	Global	*Rienecker et al.* (2011)
CFSR	1979-present	0.50° × 0.50°	6-hourly	Global	*Saha et al.* (2010)

Table 4: Annual amplitudes of various rainfall and temperature products over the Ganges and Brahmaputra-Meghna-RBs over the period 1980-2013.

Data—	Rainfall [mm/yr]		Temperature [°C]	
	Ganges	**Brahmaputra-Meghna**	**Ganges**	**Brahmaputra-Meghna**
APHRODITE [1980-2007]	260.3	263.9	-	-
GPCCv6 [1980-2007]	311.7 (310.0)	351.4 (346.3)	-	-
CRU_TS3.22 [1980-2007]	284.1 (280.4)	334.5 (330.0)	6.9	7.0
TMPAv7 [1998-2013]	320.7	330	-	-
CHIRP [1998-2013]	342.4	308.8	-	-
ERA-Interim [1980-2010]	308.8	329.2	5.6	5.3
MERRA [1980-2010]	244.2	219.4	9.0	8.7
CFSR [1980-2010]	345.4	379.5	8.2	8.4

Table 5: Linear trends in rainfall (mm/decade) derived from observations and reanalysis products. Values that are significant at 95% confidence level are highlighted in bold.

Rainfall Products—	**Ganges [mm/dec]**				**Brahmaputra-Meghna [mm/dec]**			
	Winter	Spring	Summer	Autumn	Winter	Spring	Summer	Autumn
GPCCv6 [1980-2010]	-0.7	-12	0.2	**-2.9**	-0.8	0.2	-4.5	-1.9
TRMMv7 [1998-2013]	2.1	-6.1	12.4	-6.6	-0.1	-4.6	**-39.0**	-3.3
CHIRP [1998-2013]	1.1	-2.0	-7.0	-10.3	0.0	-3.9	-20.2	-9.2
ERA-Interim [1980-2010]	-1.5	-9.5	-5.8	**-3.6**	-6.8	-12.6	-6.9	**-2.8**
MERRA [1980-2010]	1.1	9.0	3.0	-2.0	5.9	**17.4**	3.0	-1.1
CFSR [1980-2010]	-0.8	18.1	1.9	-2.1	0.9	19.8	5.0	-3.2

Table 6: Linear trends in temperature (°C/decade) derived from observations and reanalysis products. The values that are significant at 95% confidence level are shown in bold.

	CRU_TS3.22	**UDEL**	**ERA-Interim**	**MERRA**	**CFSR**
			Ganges		
Spring	**0.38**	**0.36**	0.08	0.16	**0.52**
Summer	0.1	0.03	-0.22	**-0.4**	-0.17
Autumn	**0.41**	**0.27**	0.08	0.21	**0.31**
Winter	**0.41**	**0.26**	0.32	**0.31**	**0.42**
			Brahmaputra-Meghna		
Spring	**0.42**	**0.39**	0.15	**0.26**	**0.43**
Summer	**0.21**	0.09	-0.06	0.1	0.02
Autumn	**0.46**	**0.28**	0.06	**0.28**	**0.33**
Winter	**0.64**	**0.48**	0.35	**0.43**	**0.8**

Table 7: Correlation between CRU_TS3.22 and other temperature products over the GBM RB. Correlations were computed between the PCs of first two leading modes of CRU_TS3.22 and other products.

Temperature products	**PC 1**	**PC 2**
UDEL	0.95	0.90
ERA-Interim	0.89	0.68
MERRA	0.79	0.77
CFSR	0.41	0.48

Table 8: Correlation between SST anomalies and the first two PCs of various temperature products for the period 1981 to 2010. The correlation values that are signficant at 95% confidence level are highlighted bold.

Temperature Products	**Nino3.4 vs PC 2**	**DMI vs PC 2**
CRU_TS3.22	**0.53** (at 3 month lag)	**0.24** (at 3 month lag)
UDEL	**0.56** (at 3 month lag)	**0.22** (at 3 month lag)
ERA-Interim	**0.35** (at 3 month lag)	0.05 (at 3 month lag)
MERRA	**0.46** (at 3 month lag)	0.13 (at 3 month lag)
CFSR	**0.27** (at 3 month lag)	**0.30** (at 3 month lag)

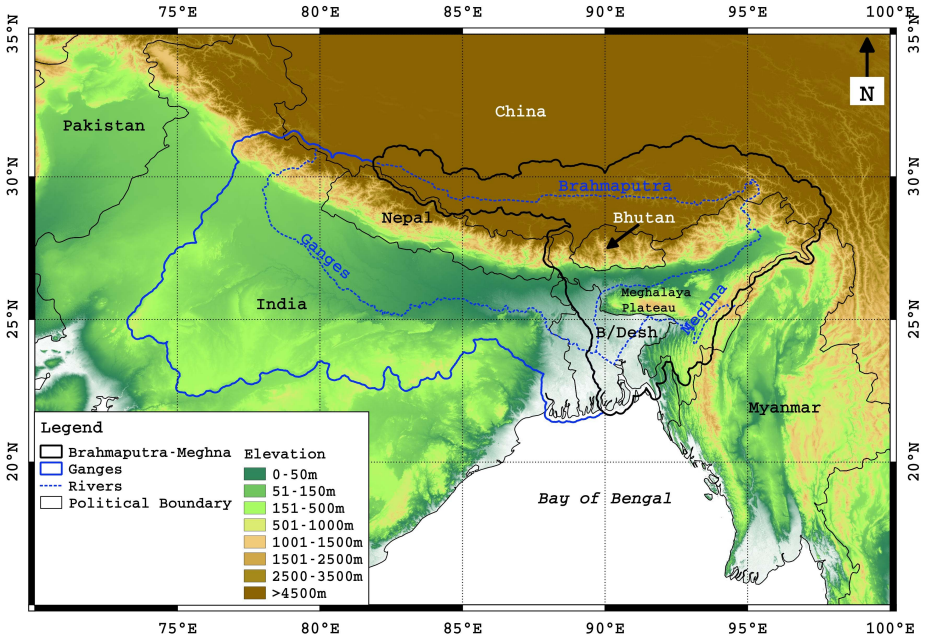

Figure 1: Overview of the Ganges-Brahmaputra-Meghna RB in South Asia. Brahmaputra and Meghna RBs are merged together, which is represented by the thick black polygon, while the Ganges River Basin is shown in thick blue polygons. This representation will be used for the remainder of this study. Source: *Khandu et al.* (2016b).

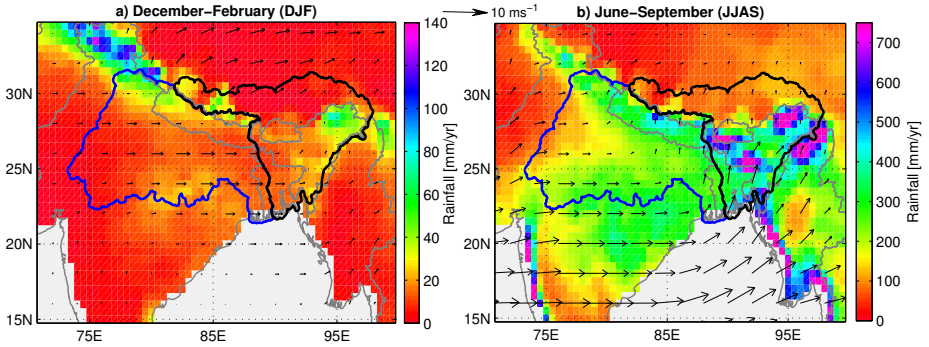

Figure 2: a) winter (DJF) and (b) monsoon (JJAS) rainfall climatology (1980–2010) based on GPCCv6 precipitation analysis over the GBM RB. The temporal mean wind fields at 850 hPa level obtained from ERA-Interim was also plotted to show the directions of winds during the two seasons.

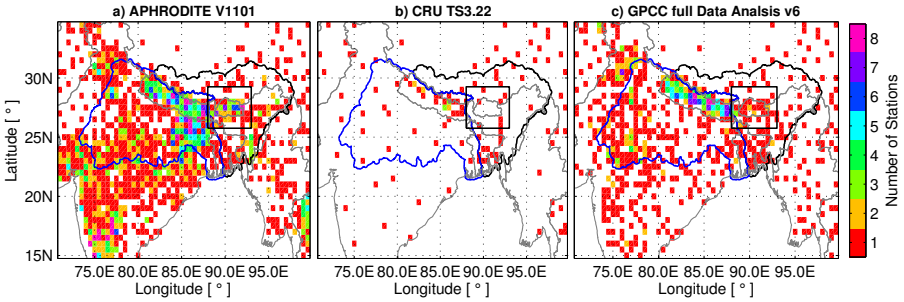

Figure 3: Spatial distribution of rain gauge stations across the GBM RB and its neighbouring regions that were used in (a) APHRODITE, (b) CRU_TS3.22, and (c) GPCCv6. Modified from *Khandu et al.* (2016a).

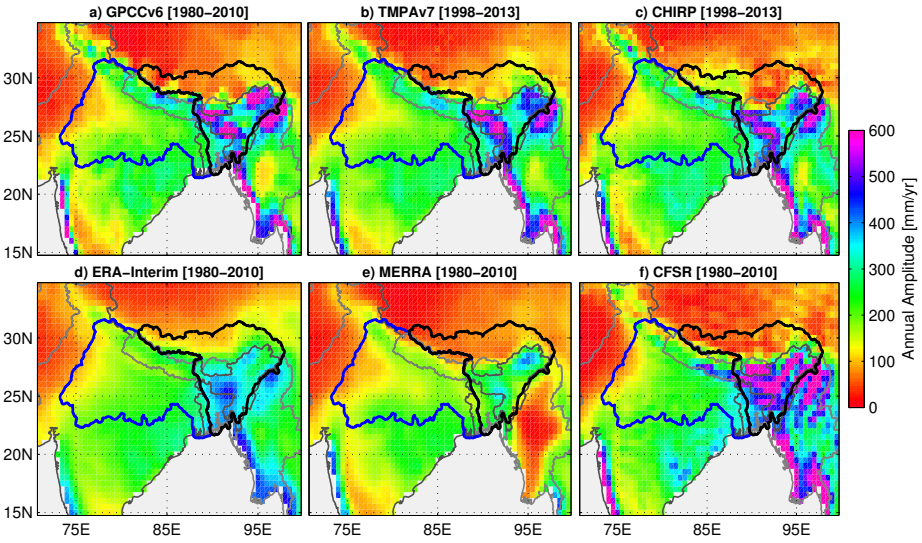

Figure 4: Spatial variations of mean annual amplitudes of monthly rainfall over the GBM RB based on a) GPCCv6 (1980–2010), (b) TMPAv7 (1998–2013, c) CHIRP (1998–2013), d) ERA-Interim (1980–2010), e) MERRA (1980–2010), f) CFSR (1980–2010)..

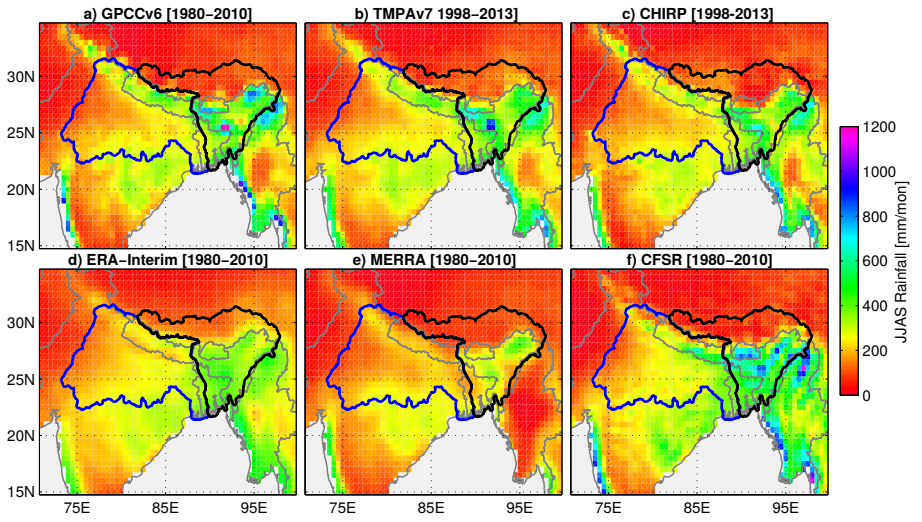

Figure 5: Spatial distribution of monsoon (JJAS) rainfall over the GBM RB a) GPCCv6 (1980–2010), (b) TMPAv7 (1998–2013, c) CHIRP (1998–2013), d) ERA-Interim (1980–2010), e) MERRA (1980–2010), f) CFSR (1980–2010).

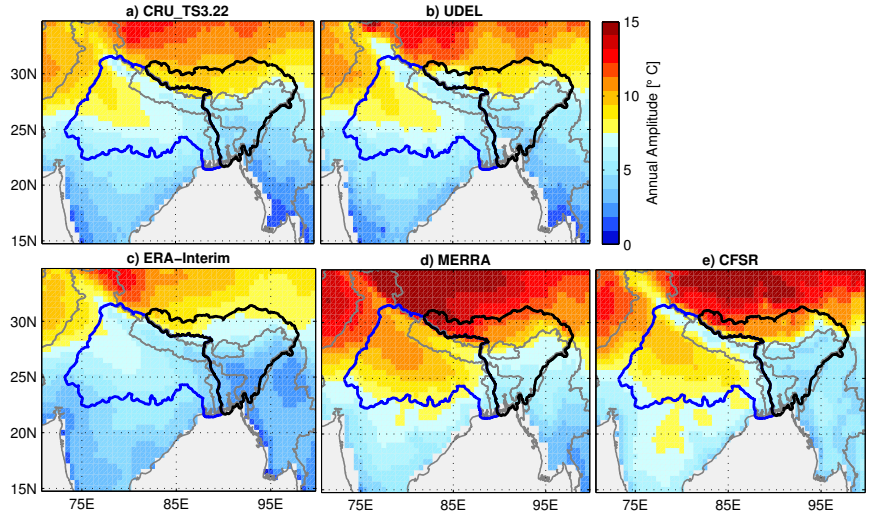

Figure 6: Spatial patterns of annual amplitudes of temperature over the GBM RB based on a) CRU_TS3.22, b) UDEL, c) ERA-Interim, d) MERRA, and e) CFSR for the period 1980–2010.

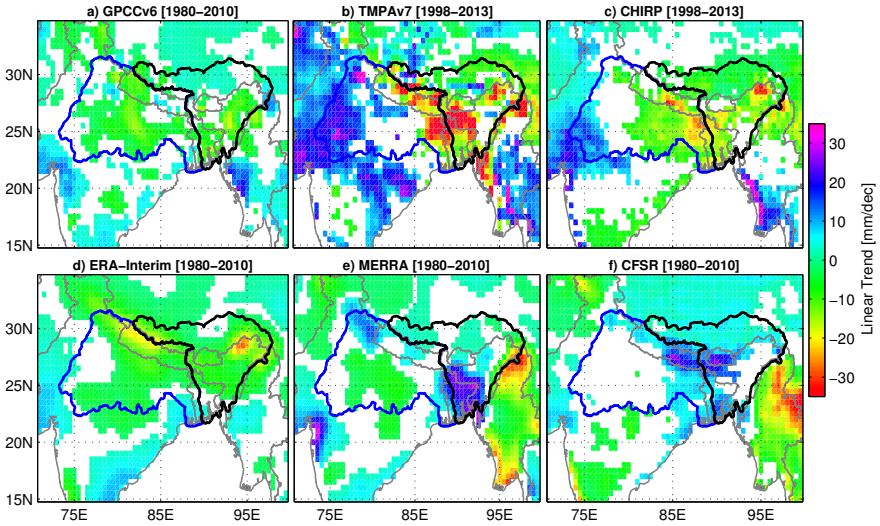

Figure 7: Precipitation changes over the GBM RB based on a) GPCCv6 (1980–2010), (b) TMPAv7 (1998–2013, c) CHIRP (1998–2013), d) ERA-Interim (1980–2010), e) MERRA (1980–2010), f) CFSR (1980–2010). Trend values that are not significant at 95% confidence level are masked out.

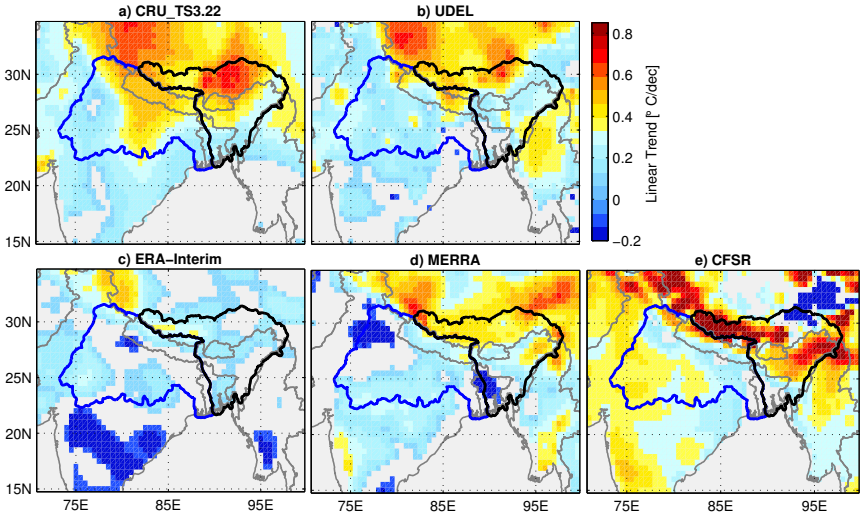

Figure 8: Spatial variation of temperature trends based on a) CRU_TS3.22, b) UDEL, c) ERA-Interim, d) MERRA, and e) CFSR for the period 1980–2013 in the GBM RB. Trend values that are not significant at 95% confidence level are not shown.

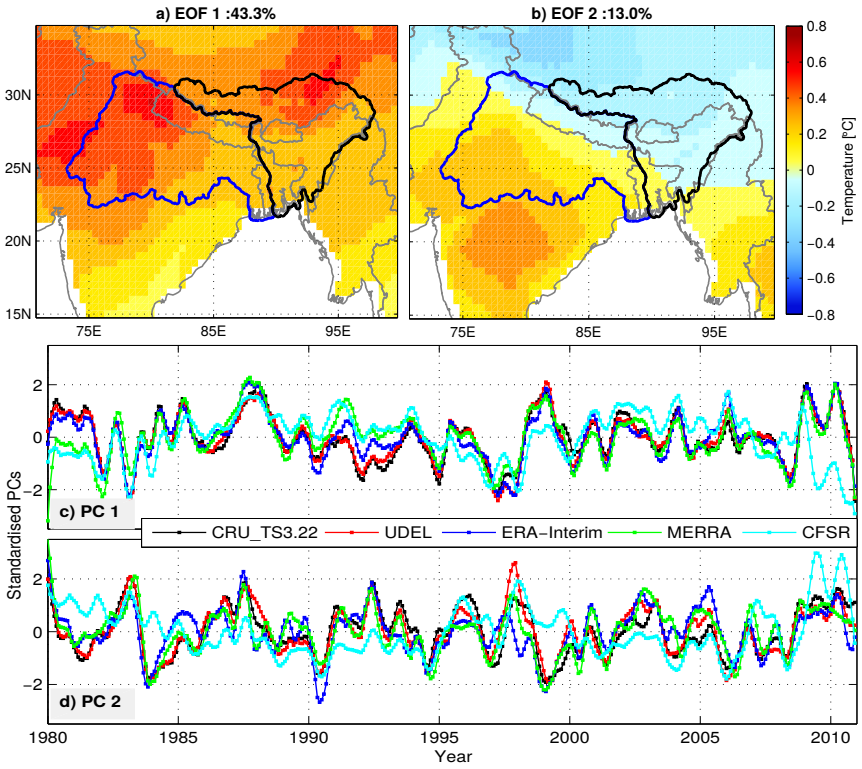

Figure 9: Spatial patterns or EOFs (a & b) and temporal components or PCs (c & d) based on first two leading modes of PCA analysis on monthly temperature anomaly of CRU_TS3.22 over the period 1980–2013. PCs of UDEL, ERA-Interim, MERRA, and CFSR indicated in c & d are derived by projecting their respective anomalies onto the EOFs of CRU_TS3.22.

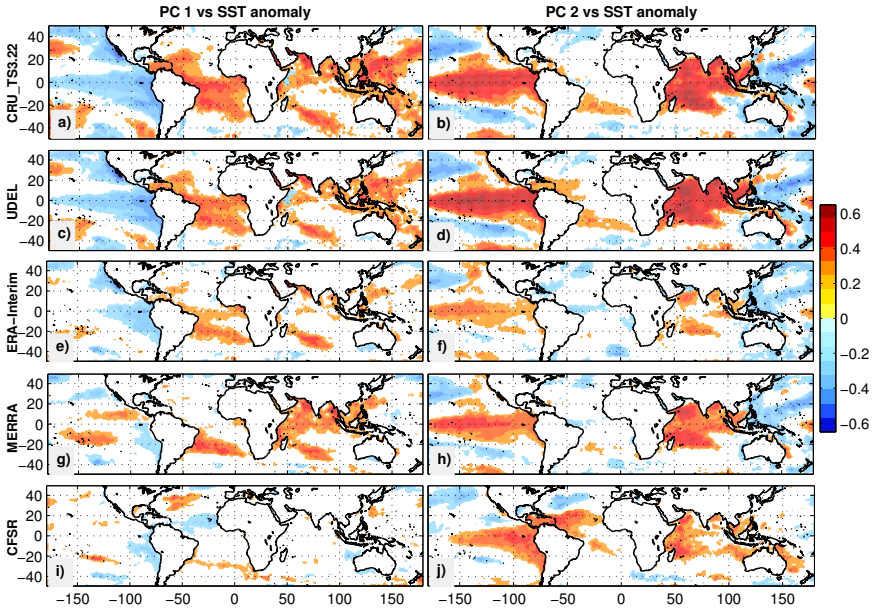

Figure 10: Correlation between the temporal components (PC 1 and PC2) and monthly SST data of HadSST over the period 1980–2013.

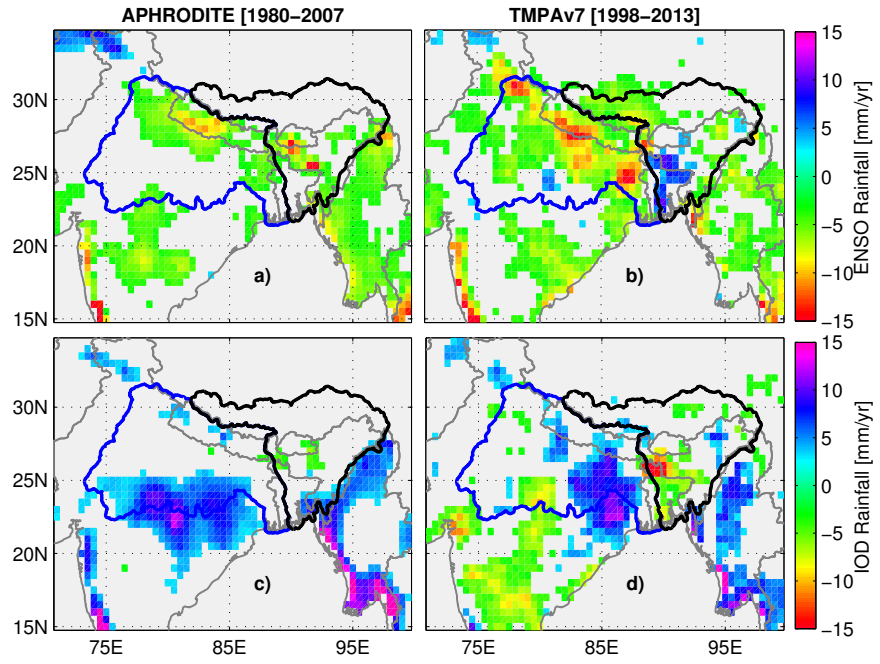

Figure 11: Regression of Niño3.4 index and DMI on precipitation anomalies of APHRODITE (1980-2007) and TMPAv7 (1998-2013). Values that are not significant at 95% confidence level based on student's t-test are not shown.

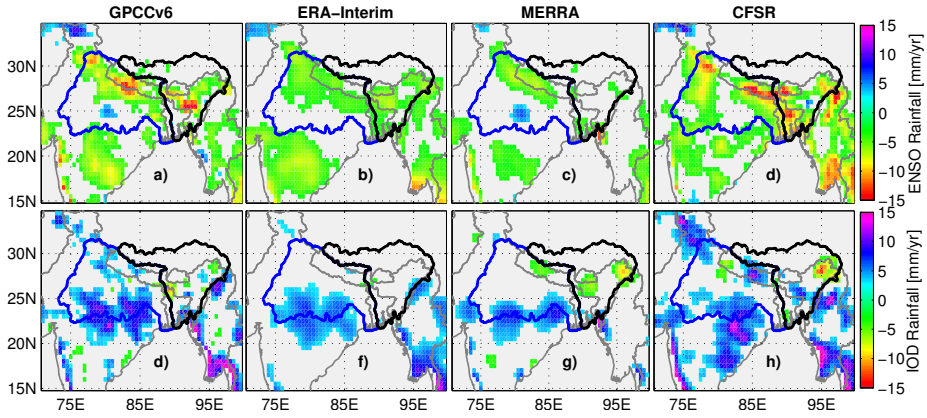

Figure 12: Regression Niño3.4 index and DMI on the precipitation anomalies of GPCCv6 and reanalysis products for the period 1980-2010. Precipitation contributions that are not significant at 95% confidence level based on student's t-test are not shown.